

Unveiling the spontaneous conversion of layered MAX phases to 2D MXenes

Author Information

Tao Hu^{1,2†}, Shihao Zhu^{1†}, Zhaojin Li^{1,3}, Da Li¹, Hongyang Liu¹, Chao Zhang¹ & Xiaohui Wang^{1*}

Affiliations

¹Shenyang National Laboratory for Materials Science, Institute of Metal Research, Chinese Academy of Sciences, Shenyang, China

²Institute of Materials Science and Devices, College of Materials Science and Engineering, Suzhou University of Science and Technology, Suzhou, China

³College of Materials Science and Engineering, Hebei University of Science and Technology, Shijiazhuang, China

Contributions

T.H. conducted the DFT calculations, built the model, and wrote the manuscript. S.H.Z. and Z.J.L. conducted the etching experiment. C.Z. prepared the MAX phases precursor. X.H.W. supervised the project and edited the manuscript.

Corresponding author

Correspondence to: wang@imr.ac.cn, Xiaohui Wang

ORCID ID: 0000-0001-7271-2662.

Abstract

Topochemically transforming layered non-van der Waals solid into two dimensional (2D) materials involves selective etching reactions with atomic precision. The element-specific, structure-sensitive

etching at nanoscale urgently requires in-depth understanding. Here, by means of density functional theory calculations and a laboratory-made operando reaction monitoring platform, the mechanism of instantaneous transforming MAX phase into MXenes is unraveled. The overall etching kinetics exhibits a sigmoidal curve, following self-accelerating reaction character with a small activation energy of *ca.* 60 kJ/mol. Interestingly, this activation energy corresponds to the Al transport through Ti_3C_2 slits. Therefore the reaction of Al with hydrofluoric acid solution in the confined interlayer space is recognized as the rate-determining step. Last but not the least, we found that the match of A element and etchants to form stable products is critical for the etching reaction, and reaction energy derived from the thermodynamics provides an easy yet effective descriptor for screening efficient etchants.

Introduction

Topochemically etching off specific element from covalently bonded layered compounds is a promising strategy for developing novel 2D materials.¹ Such an exfoliation method leads to the synthesis of a series of atomically-thick metastable materials with unique structures and has achieved triumph in two-dimensional transition metal carbides/nitrides (MXenes)² and borides (MBene)³⁻⁵. This is hardly achieved by conventional method. Topochemical etching method traces its history to the synthesis of silicon nanosheets and other Si-based nanomaterials years ago.^{6,7} Though topochemical etching has enabled many 2D materials from layered non-van der Waals compounds, the mechanism of the etching process is seldom treated. Topochemical conversion of non-van der Waals solids to 2D materials is of increasing significance which requires in-depth understanding.⁸ Despite of the importance in 2D material synthesis, the etching with atomic precision is also a promising strategy for atomic and close-to-atomic scale manufacturing.

MXene is one of the most extensively and intensively studied 2D materials after graphene.¹ Holding promise in various applications such as energy storage,^{9,10} energy transformation,¹¹ and electromagnetic shielding materials,¹² MXenes have been attracting increasing attentions since they were first introduced by topochemical etching strategy.¹³ Generally, the MXenes can be produced by selectively etching off the

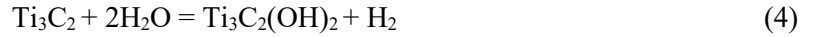
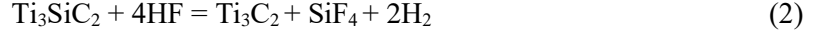
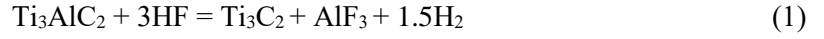
A elements from MAX phases wherein A element layers are sandwiched by covalent MX layers (M represents early transition metal, A is group III A or IV A element, and X is C and/or N).^{14,15} This process can also be realized by polar organic solvents etching,^{16,17} anodic etching,^{18,19} element replacement by reaction with Lewis acidic molten salts,^{20,21} or hydrothermal etching strategy.²² Topochemical reaction is so important that it is currently the only effective approach to many novel 2D materials obtained from non-van der Waals solids. Besides, there are more layered non-van der Waals solids have not been exfoliated yet. The limit knowledge of topochemical reaction and inefficient trial-and-error have hindered the development of this method. Moreover, the kinetics for the selective chemical etching process remains unclear, which greatly attracts our interests.

In this work, by means of a combination of DFT calculations and operando experiment, we present an atomistic understanding of the topochemical reaction by taking selectively etching of Ti_3AlC_2 in HF aqueous solution as an example. The main contents are designed as following: First, bonding and energetics of Ti_3AC_2 (A=Al and Si) MAX phases were closely checked. Then thermodynamics of A extraction and MX functionalization, as well as detailed kinetics were evaluated for etching of MAX phases. Next, based on the online monitoring of gas species and volume during etching process, reaction kinetics was worked out. Last but not the least, reaction energy was recognized as an effective descriptor of selective etching. We believe the study would impact on three aspects: (i) elucidating the mechanism of topochemical transition of MAX phases towards MXenes; (ii) atomistic understanding of topochemical reactions; and (iii) guiding the selection of efficient etchants.

Results

Bonding and energetics of Ti_3AC_2 (A=Al and Si) MAX phases. According to previous studies,¹³ the Al atom layer sandwiched by Ti_3C_2 layers is able to react with HF solution, generating H_2 molecules and resulting in Ti_3C_2 MXene (equation 1). Ti_3SiC_2 can also be etched by HF solution combined with oxidant

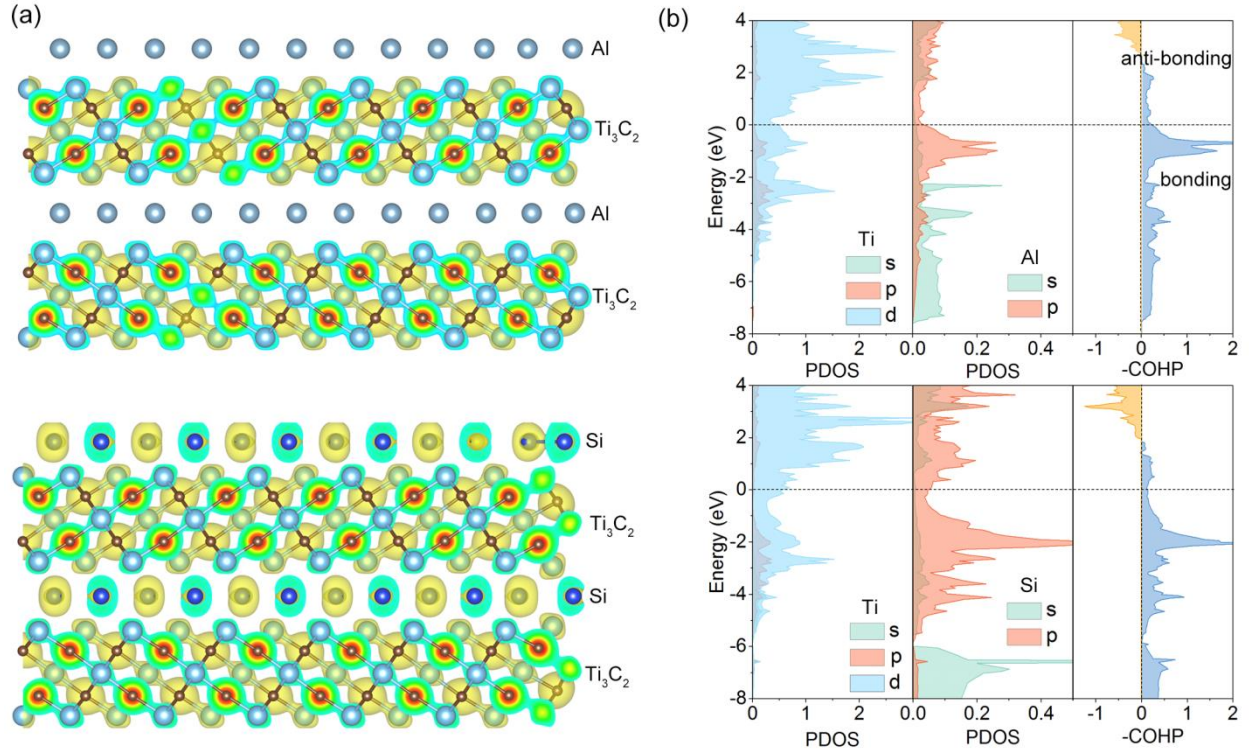
assistantance.²³ For comparison, the hypothetical chemical reaction of HF and Ti_3SiC_2 (equation 2) resembling HF etching Ti_3AlC_2 , is also considered here. The bare Ti_3C_2 layers with dangling bonds on the surface can combine HF or H_2O to form functional groups on the surface according to the formulas (3–5).



The extraction of A element (equations 1 and 2) is the essential reaction as the first step. Termination reactions (3–5) are listed but not limited to the above because recent study has demonstrated that the surface of MXenes can be covalently modified by chlorine, bromine and tellurium.²⁴ During Al extraction reaction step (equation 1), 1 mol Ti_3AlC_2 produces 1.5 mol H_2 . By $-\text{F}$ or $-\text{OH}$ (equations 3 or 4) termination, 1 mol Ti_3C_2 produce 1 mol H_2 , while by $-\text{O}$ termination, 1 mol Ti_3C_2 produce 2 mol H_2 (equation 5). Thus, completely transforming 1 mol Ti_3AlC_2 to $\text{Ti}_3\text{C}_2\text{F}_2$ or $\text{Ti}_3\text{C}_2(\text{OH})_2$ produce 2.5 mol H_2 , while transforming 1 mol Ti_3AlC_2 to $\text{Ti}_3\text{C}_2\text{O}_2$ produce 3.5 mol H_2 . In accordance with the above results, completely etching 1 mol Ti_3AlC_2 should generate *ca.* 2.5–3.5 mol H_2 (corresponding to a theoretical H_2 production of about 288–403 cm^3 from 1.0 g Ti_3AlC_2 at the temperature of 25 °C). In our experiment, the volume of experimentally collected H_2 ranges from 350 to 380 cm^3 per 1.0 g of Ti_3AlC_2 (temperature-dependent), agreeing well with the theoretically prediction. Besides, the O component is estimated to be about 55–80 at.%, and $-\text{F}/-\text{OH}$ constitute only 20–45 at.% in this etching protocol. Moreover, increasing etching temperature enhances the O termination process, agreeing with our previous study that O terminated $\text{Ti}_3\text{C}_2\text{O}_2$ is the most stable²⁵. Alternatively, the large proportion of O termination in the products confirms the H_2O involvement in etching reaction in aqueous solution, since water-free etching of Ti_3AlC_2 in polar organic solvents results in fluorine-rich MXene.¹⁶

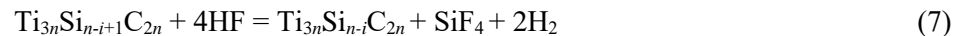
The energy change of etching Ti_3AlC_2 to Ti_3C_2 in equation 1 is -8.04 eV. While the energy change in etching Ti_3SiC_2 to Ti_3C_2 (equation 2) is only -4.48 eV. The negative reaction energies indicate that both reactions are thermodynamic feasible. The etching of Ti_3SiC_2 to Ti_3C_2 was not successful in the early studies, but was realized via an oxidant-assisted selective etching method to overcome the kinetics, confirming the thermodynamic feasibility.²³ The accumulated electron density between Si and Ti (**Fig. 1a**) shows that the Si covalently bonds with Ti, while Ti–Al is much weaker. The weak Ti–Al bonds indicate that the Al in Ti_3AlC_2 is easier to be extracted than Si in Ti_3SiC_2 . The nature of M–A bonds is coherently correlated with the electronic structures. We compared electronic structures of several typical MAX phases to be etched, i.e. Ti_3SiC_2 , Nb_2AlC , Nb_4AlC_3 , with Ti_3AlC_2 and Ti_2AlC . Surprisingly, we found that the pseudogaps of A element play key roles in the etching (Supplementary Fig. S1). The underlying physics is that the electronic density of states of A element is closely related to the reactivity. The reactivity of Al element in Ti_3AlC_2 is higher than Si in Ti_3SiC_2 (**Fig. 1b**), thus the Al is easier to be etched off. Besides, electronic structure evolution during the extraction of A atoms from Ti_3AlC_2 MAX phases clearly shows the change of electronic structures (Supplementary Fig. S2).

Fig. 1: Electronic structure of Ti_3AlC_2 and Ti_3SiC_2 .



a Electron density of Ti_3AlC_2 and Ti_3SiC_2 (100) surface (isosurface is $0.05 \text{ e}/\text{\AA}^3$). **b** Partial density of states and COHP of the Ti–A interface (A=Al, Si). The two MAX phases with identical MX layer but different A element. The M–A bond strength determines the exfoliation possibility.

Thermodynamics of A extraction and functionalization. Generally speaking, A is transported along the basal plane. To investigate the A extraction process, we focus on thermodynamics of extracting A out of Ti_3AlC_2 (100) surface to form stable A-containing compounds. Energy profiles of A element extraction was calculated by equations (6-9). **Fig. 2a-b** present the energy profiles of removing Al or Si atoms from the (100) surface to form Ti_3C_2 MXene and AlF_3 or SiF_4 .

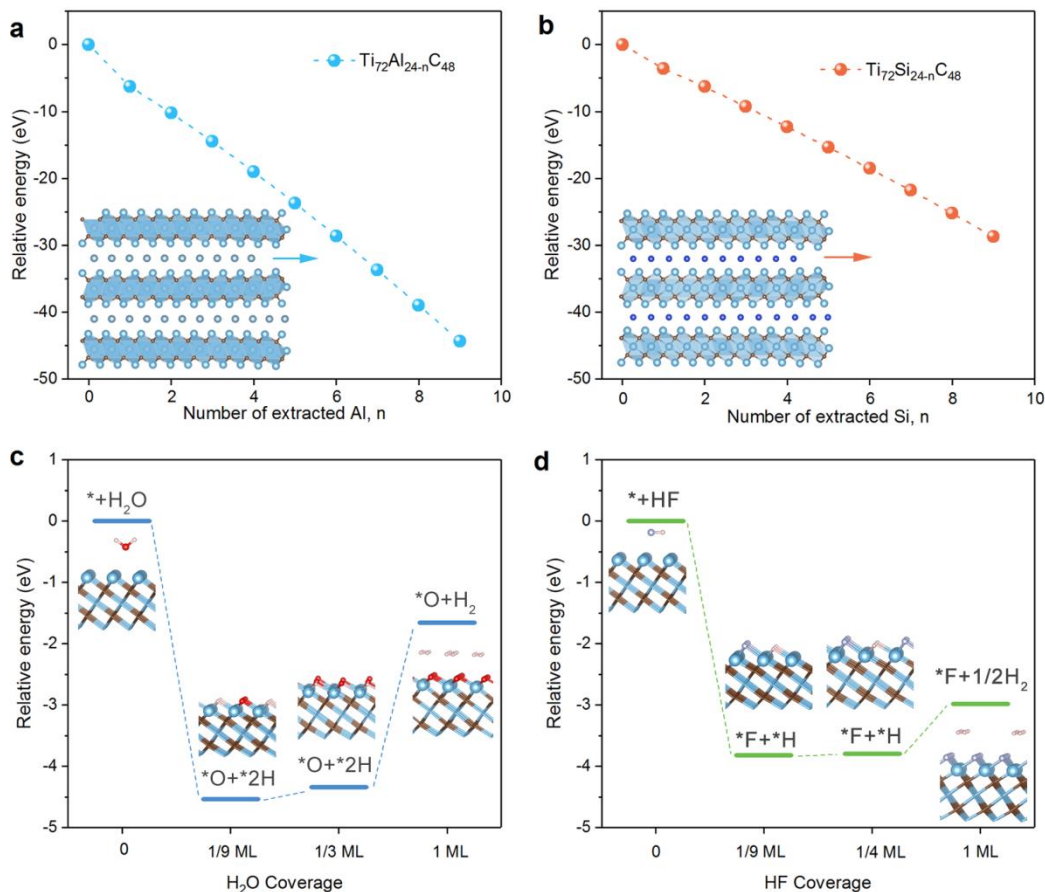


$$\Delta E(\text{Al}_i) = 2E(\text{Ti}_{3n}\text{Al}_{n-i}\text{C}_{2n}) + 2E(\text{AlF}_3) + 3E(\text{H}_2) - 2E(\text{Ti}_{3n}\text{Al}_{n-i+1}\text{C}_{2n}) - 6E(\text{HF}) \quad (8)$$

$$\Delta E(\text{Si}_i) = E(\text{Ti}_{3n}\text{Si}_{n-i}\text{C}_{2n}) + E(\text{SiF}_4) + 2E(\text{H}_2) - E(\text{Ti}_{3n}\text{Si}_{n-i+1}\text{C}_{2n}) - 4E(\text{HF}) \quad (9)$$

The decreased total energy of the system indicates both Al and Si extractions are thermodynamically feasible process. Intercalation of H₂O and HF into the gallery spacing of inorganic layered materials²⁶ may lead to termination reaction. Three kinds of H₂O/HF coverage models were built to investigate the termination process. **Fig. 2c** and **2d** show 1 monolayer coverage of H₂O or HF molecules split on Ti₃C₂ monolayer respectively. The result demonstrates that low and medium concentration H₂O and HF split into adsorbed –O, –F, and –H on Ti₃C₂ monolayer. Besides, high concentration H₂O or HF results in –O or –F termination and H₂ gas. The experimentally collected H₂ partially comes from H⁺ reduction by accepting electrons from Al (equation 1), and extra H₂ from H⁺ reduction by accepting electrons from Ti₃C₂ in the termination process (equation 3-5). Recalling the distinct behaviors of Ti₃AlC₂ and Ti₃SiC₂ in hydrofluoric acid, it is reasonable to believe that the extraction of A is the rate-determining step. Extraction of A atoms from MAX phase is the rate-determining step, as the reaction between H₂O or HF and Ti₃C₂ is simultaneous, which will be shown in the following passage.

Fig. 2: Energy profiles of *A* extraction, and H₂O/HF splitting on Ti₃C₂ monolayer.

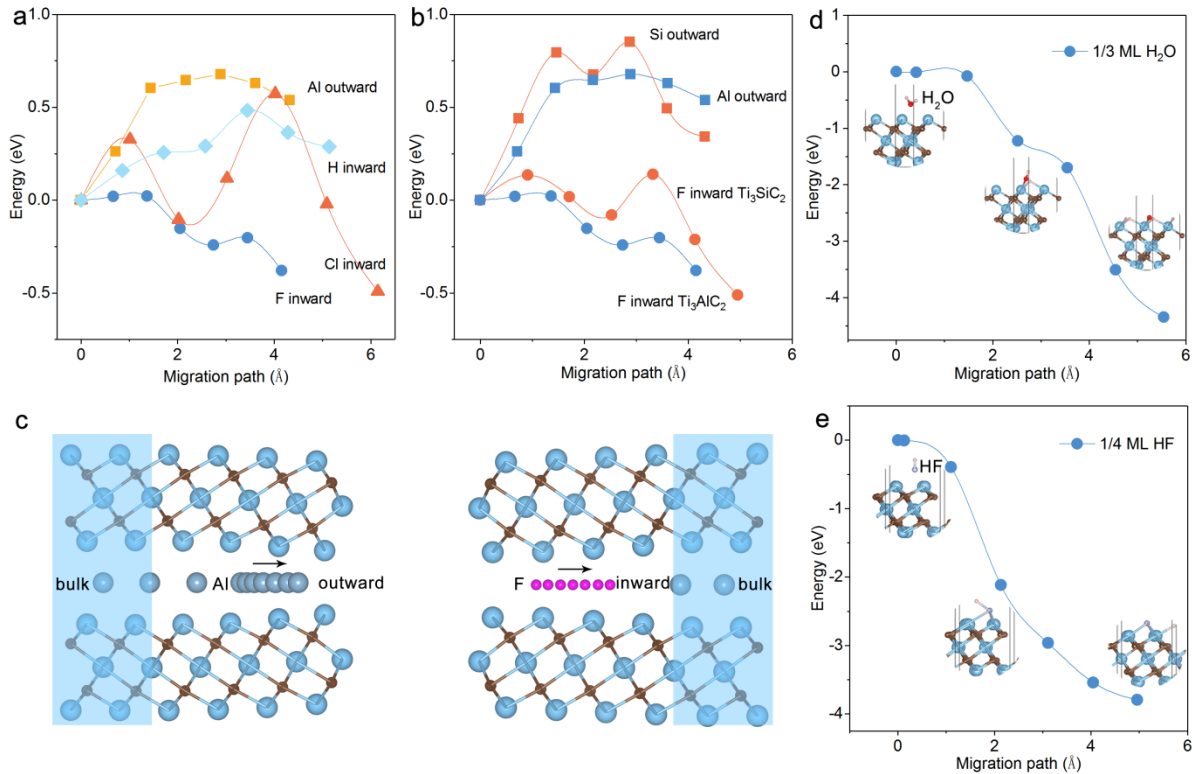


a Al extraction from Ti₃AlC₂ to form AlF₃. **b** Si extraction from Ti₃SiC₂ to form SiF₄. **c** H₂O interacts with Ti₃C₂ basal surface. **d** HF interacts with Ti₃C₂ basal surface. The most stable structures of AlF₃ and SiF₄ from Materials Projects are used as reference.²⁷

Kinetics analysis for etching of MAX phases. Though the *A*-extraction reactions in Ti₃AlC₂ and Ti₃SiC₂ are exothermic reaction, the activation energies of the *A* extraction process is needed to be considered. As shown in **Fig. 3**, the energy barrier for Al migration from inner site outward along basal plane is calculated to be 0.64 eV in Ti₃AlC₂. This kinetic result is in agreement with previous report²⁸, where the adjacent Al migrates to the edge site in MAX phases. Interestingly, the activation energy based on experiment is coincided about 60 kJ/mol (0.62 eV per molecule). This result also rationalize the collapsed nano arches at edges experimentally observed in Ti₃AlC₂ etched by hydrofluoric acid.²⁹ The energy barrier for Si migration is higher than that of Al, indicates the sluggish kinetics of Si extraction.

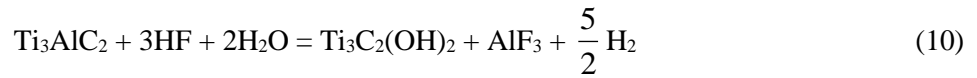
Considering the equilibrium in aqueous hydrofluoric acid solution: $\text{HF}_2^- = \text{HF} + \text{F}^-$,³⁰ F^- diffusion into the interlayer of Ti_3AlC_2 was considered for the sake of convenience. To keep charge neutrality in the local environment, atomic F was used in the NEB calculations. Fluorine has the lowest migration barrier in the confined space between the Ti_3C_2 layers, as evidenced by the NEB results in Fig. 3a. Generally, the atomic migration barrier in Ti_3AlC_2 increases with increasing atomic radii.³¹ The fluorine ion migration barrier in Ti_3SiC_2 is higher than that in Ti_3AlC_2 , due to the smaller interlayer space in Ti_3SiC_2 (3.96 Å) than that in Ti_3AlC_2 (4.56 Å, Supplementary Fig. S3). For Ti_3SiC_2 , the Si migration is rather rough without oxidant. Given the oxidant-assistance Ti_3SiC_2 etching, it is reasonable to propose that Si in the MX interlayer first loses electrons and is oxidized to Si^{4+} in strong oxidizing circumstance (as evidenced by the high electrostatic potential around Si-Ti bonds, in Supplementary Fig. S4). The Si^{4+} ionic radius (0.26 Å) is much smaller than Si atomic radius (1.10 Å), thus rendering the Si^{4+} extraction and sustainable selective etching, which requires further detailed study. The results of transition state calculations are included in Supplementary Fig. S5-11.

Fig. 3: Kinetics of mass transport at nanolamellar tunnel in MAX phases by NEB.

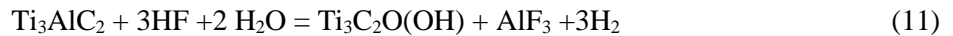


a Energy barriers of atomic species migration in Ti_3AlC_2 . **b** Comparison of A outward migration and F inward migration in Ti_3AlC_2 and Ti_3SiC_2 . **c** Schematic of A outward migration and F inward migration. **d** Energy minimum path of Al migrates outward and F migrates inward of Ti_3AlC_2 (100) surface. **e** Medium concentration of HF molecules split on Ti_3C_2 monolayer. **f** Medium concentration of H_2O molecules split on Ti_3C_2 monolayer. Note that low and middle concentration H_2O and HF split on Ti_3C_2 monolayer in terms of adsorbed $-\text{O}$, $-\text{F}$, and $-\text{H}$. High concentration H_2O or HF result in $-\text{O}$ or $-\text{F}$ termination and H_2 gas.

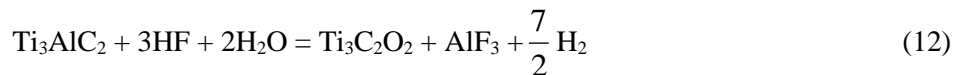
Online monitoring of etching process by gas identification and collection. Using the lab-made gas identification and monitoring devices, the gas produced during etching was identified to be H_2 (see Supplementary Fig. S14-15). Then we studied the etching kinetics of porous Ti_3AlC_2 monolith by using the produced H_2 as an indicator. A set of experiments were performed at varied temperatures, using aqueous HF solution with fixed concentration. To minimize the measurement error that may arise from the highly exothermic reaction and to keep the HF concentration relatively fixed during the entire etching process, excessive HF was used. **Fig. 4** presents the hydrogen gas profiles of porous Ti_3AlC_2 monolith exposed to abundant HF solution (50%). Specifically, the volume of H_2 gas evolved at 40 °C was experimentally collected to be 356.8 cm^3 at 25 °C. According to overall equations 10-12, the theoretical H_2 volumes are 314.7, 377.7 and 440.6 cm^3 at 25 °C, depending on the resultant of $\text{Ti}_3\text{C}_2\text{T}_x$ MXene with distinct functional terminations. At the same time, the increased temperature could boost the O termination process and generate more O termination.



(314.7 cm^3 H_2 per gram of Ti_3AlC_2)



(377.7 cm^3 H_2 per gram of Ti_3AlC_2)

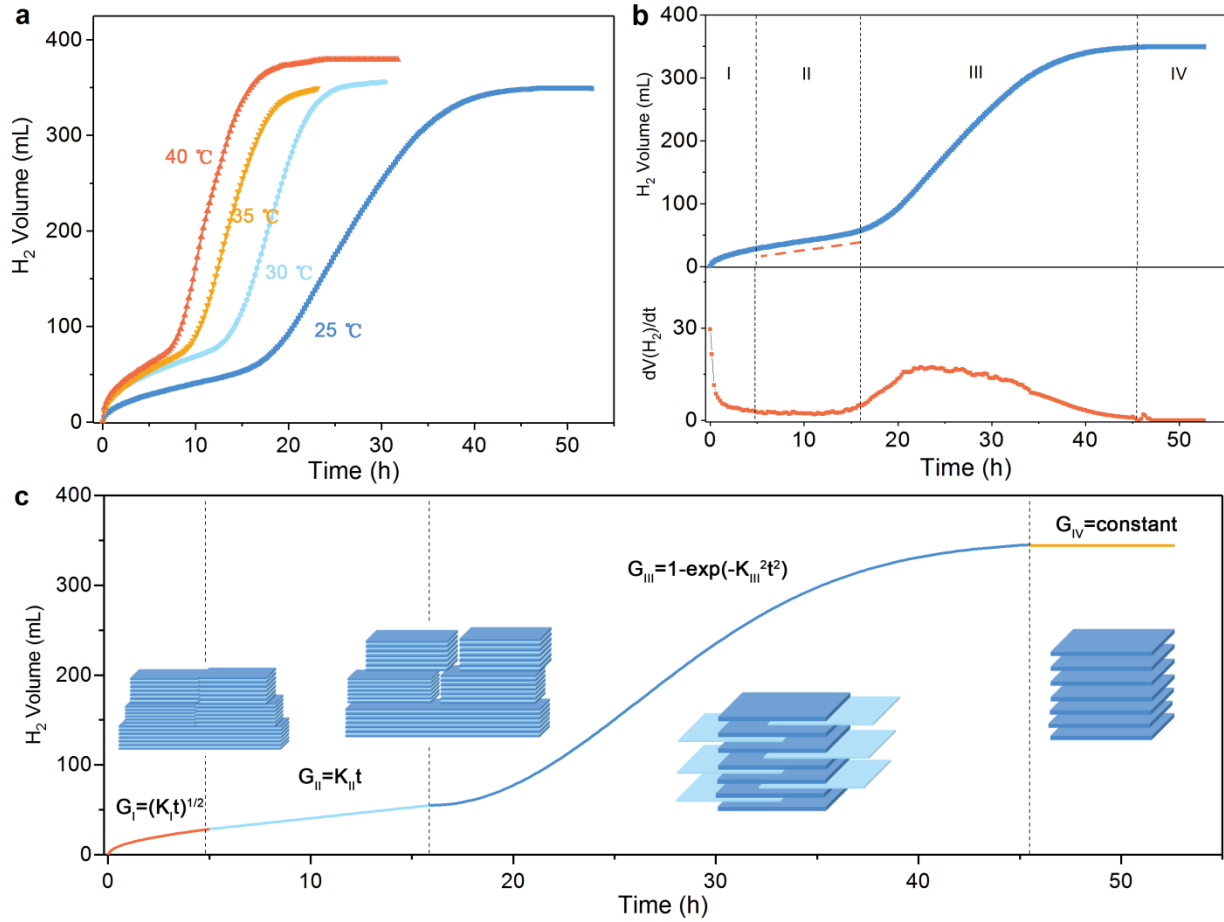


(440.6 cm³ H₂ per gram of Ti₃AlC₂)

Then the amount of H₂ was used to deduce the possible reaction mechanism. F-terminated reaction is not presented in the reaction equations because –F is isoelectric with –OH. These isoelectric terminations give rise to equal amount of hydrogen. In the case of OH-terminated or F-terminated Ti₃C₂T_x MXene, the theoretical volume of H₂ evolution is only 314.7 cm³ per gram of Ti₃AlC₂, while the volume approaches as high as 440.6 cm³ per gram of Ti₃AlC₂ for Ti₃C₂O₂ MXene. The experimentally determined volumes are in the range of these volumes, confirming that the terminations consist of –O and –OH/–F mixture.³² This is in line with the well-accepted knowledge on the termination composition of Ti₃C₂T_x MXene.

Reaction kinetics analysis. Etching experiment at four different temperatures shows some common features. As shown in **Fig. 4**, the H₂ evolution profile signifies the overall etching process follows a sigmoidal curve (S-curve). The S-curve has been widely used to model the natural life cycle of many things, from bacteria flora growth, to population growth, and recently found in crystal growth kinetics³³. The curve is basically a stretched out S shape lying on its side, and can be thought of as having several sections, each of which corresponds to a phase of etching. To quantitatively understand this process, we deduced the possible reaction models (Part III Etching reaction models in Supplementary Information). We found that neither the conventional reaction-controlled model nor diffusion-controlled model in solid-state reactions can explain the S-shape kinetics curve during the selective etching. Insights can be obtained by combining the H₂ evolution curves at four temperatures and their derivative curves. The online gas evolution monitoring data definitely reveals that the etching process includes four well-separated steps: the pre-etching period (stage I), initial etching of the monolith through grain boundary and dissociation of the monolith into individual grains (stage II), burst etching of individual Ti₃AlC₂ grains (stage III), and completion of the etching (stage IV). Then the experimental data in each stage is used to fit the models and find out the most probable model. The best-fitted models are presented in **Fig. 4c**.

Fig. 4: Four stages of Ti_3AlC_2 MAX phase etching reactions.



a Online H_2 monitoring of hydrofluoric acid (40%) etching Ti_3AlC_2 at 25 °C, 30 °C, 35 °C, 40 °C . **b.** H_2 evolution at 25 °C and its derivative. **c.** Modeling results and schematic illustration of etching process of MAX phases. Four insets are (I) pre-etching process, (II) induction period, (III) accelerating period, and (IV) completion of etching respectively.

In the pre-etching process (stage I): the solution contacts with the outmost surfaces. The best-fit model is parabolic model which is usually seen in membrane oxidation governed by gas diffusion. The relatively high reaction rate means this is a fast process. The produced H_2 in this stage most probably comes from the process that exposed Al atoms are etched off and the outmost Ti layers of Ti_3AlC_2 particles are functionalized. The reaction between etchant and outmost Al or Ti layers is easy and this process is

controlled by the diffusion of solution. Interestingly, stage II (induction period) follows a linear kinetics at varied temperatures. In this period, the etchant solution comes into the grain boundaries, resembling the siphonage. The best-fitted model is constant liquid-solid interface shift velocity model (Part III in ESI), in which the H_2 amount increases linearly with the liquid-solid interface shift. In this process, the reaction rate is relatively low due to the limited spacing and reactants. Stage III exhibits self-accelerating feature. After the polycrystal divided into small individual grains, each small grain gets full contact with etchants and multilayer Al react with etchants at the same time. This period reflects mainly the intrinsic etching process. The activation energy in this stage corresponds to the intrinsic activation energy of etching reaction. The drastic increase of reaction rate in this period is mainly attributed to the burst of number of Al layers reaction with etchants. The autocatalytic feature was also found in thermo decomposition of transition metal formates and carboxylates.³⁴ Stage IV is the completion of etching.

Quantitative analysis of the reaction rate at the sigmoidal curves reveals the kinetic mechanism.³³ Stage III is selected to determine the activation energy of etching Ti_3AlC_2 grains by HF solution. The Avrami-Erofeev equation was used to fit the III period.

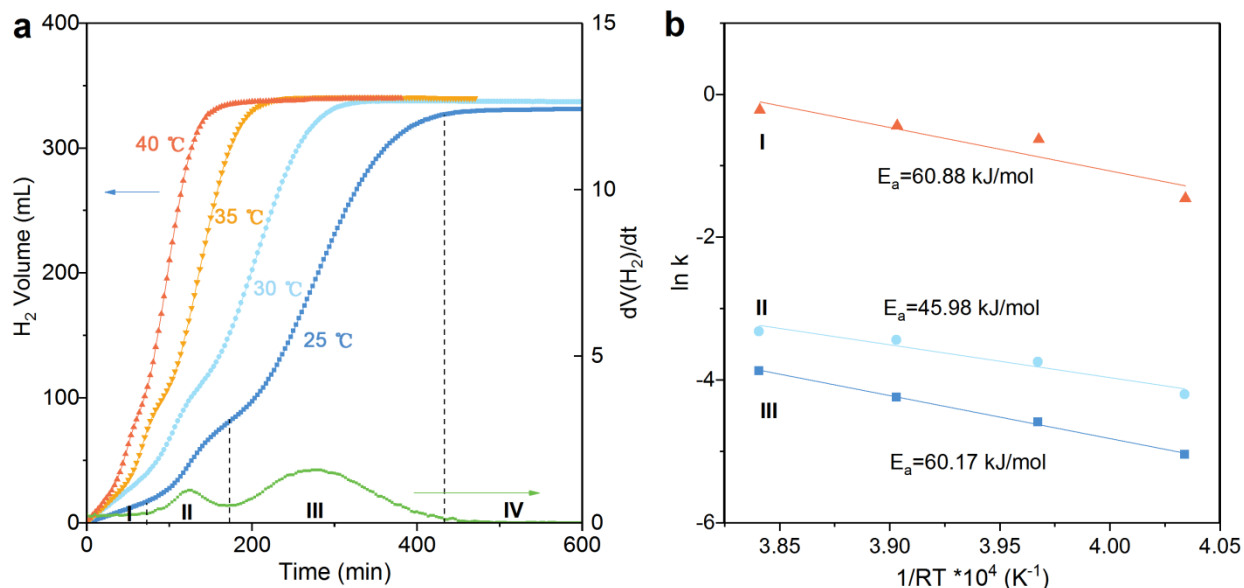
$$-\ln(1-G) = k^2 t^2 \quad (13)$$

The dependence of reaction rate constant, k , on the reaction temperature, T , can be described by Arrhenius equation:^{33, 35}

$$k = Ae^{-E_a/RT} \quad (14)$$

where R , A , and E_a represent the universal gas constant ($8.314 \text{ J mol}^{-1} \text{ K}^{-1}$), the frequency factor, and the apparent activation energy, respectively. From the temperature-dependent etching kinetics, the apparent activation energies (E_a) for the stage III is determined to be 60.17 kJ/mol (**Fig. 5b**). This is very close to the calculated activation energy of Al migration outward by DFT calculations (61.5 kJ/mol , about 0.64 eV/atom). Again, this result proved that the migration of Al in the interlayer space plays key roles in the etching kinetics.

Fig. 5: Four stages of Ti_3AlC_2 MAX phase etching reactions. Determination of activation energies.



a Online H_2 monitoring of hydrofluoric acid (50%) etching HCl-treated Ti_3AlC_2 at 25 °C, 30 °C, 35 °C, and 40 °C. H_2 evolution at 25°C and its derivative are used to indicate the four stages of etching reaction.

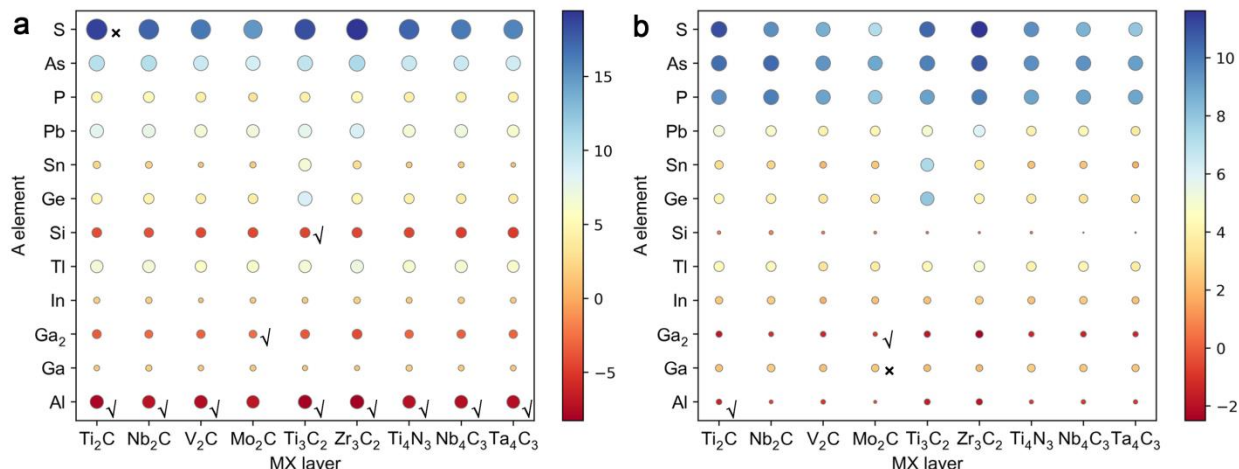
b Linear fitting of $\ln(k)$ as a function of $1/RT$, in which the slope of linear regression line can be used to calculate the corresponding reaction activation energy (E_a) using the Arrhenius equation. The dotted vertical lines in panel **a** highlight the typical reaction stages (I, II, III, and IV). Etching process can be accelerated by gentle heating.³⁶ It has to be admitted that, this study is based on the assumption that the kinetics of gas evolution reflects the kinetics of etching of MAX phases.

Reaction energy as a descriptor

Whether a MAX phase can be etched in a certain solution on one hand is related with the structure of the material itself, but on the other hand depends on the etchant. Previous work attributed the successful exfoliation of such materials to the intrinsic weak interlayer bonding,³⁷ but encouraging communications with experimental colleagues inspired us that the match of materials and etchant may be the key point. Therefore, we selected nearly one hundred typical MAX phases (9 different MX layers and 11 A elements),³⁸ two main etchants (hydrofluoric acid and hydrochloric acid) in literature² and calculated the

reaction energy of etching reactions. After a systematical comparison with available experimental results, we found the reaction energy is an intriguing descriptor of the etching behavior.

Fig. 6: Heat maps of reaction energies in etching MAX phases by hydrofluoric and hydrochloric acids.



a. Reaction energies of MAX phases and hydrofluoric acid. **b.** Reaction energies of MAX phases and hydrochloric acid. Some experimental results are indicated. The tick ✓ marks the successful etching and cross × marks the failure of etching.

As shown in **Fig. 6**, the MAX phases with the same A element show similar reaction energies with etchants. The etching possibility mainly depends on the activity of A element, as well as whether A element and etchants can produce stable products. It is found the reaction energy is an easy but effective descriptor to predict the etching possibility. The heat map clearly shows that MAX phases with A=Al or Si are the easiest to be etched in hydrofluoric or hydrochloric acids. Most of the Al-containing MAX phases have been successfully etched by hydrofluoric acid. Mo₂AlC could also be etched by hydrofluoric acid if it is synthesized. According to previous experimental work, Mo₂C MXenes were synthesized from Mo₂Ga₂C other than Mo₂GaC.²² This is rationalized by the reaction energies of Mo₂GaC and Mo₂Ga₂C. The former with a positive reaction energy and the latter with a negative one, demonstrating that reaction energy is an effective descriptor, as shown in **Fig. 6**. Moreover, the negative reaction energy of Mo₂Ga₂C and hydrochloric acid signifying that Mo₂Ga₂C can also be etched by hydrochloric acid, which has been validated by experiment recently. The HCl-based etchant has been successfully used in not only double-

Ga MAX phases³⁹ but also in Al-containing MAX phases^{22, 40}. Etching Si-containing MAX phases by hydrofluoric acid is feasible based on the reaction energy and this has been realized by an oxidation-assistant selective etching method.²³ Experimental trials to etch Ti_2SC by hydrofluoric acid result in not Ti_2C MXene but sulfur carbide SC_x nanosheet.⁴¹ Interestingly, the results here clearly shows that the transformation of Ti_2SC to Ti_2C MXene in hydrofluoric acid is thermodynamically unfavorable. As is shown, reaction energy is a convenient descriptor of etching possibility with robustness.

Discussion

In summary, we have elucidated the mechanism of topochemical reaction of preparing $\text{Ti}_3\text{C}_2\text{T}_x$ MXene from Ti_3AlC_2 precursor in hydrofluoric acid by means of a combination of DFT calculations and operando observation. The etching possibility mainly depends on the activity of A element, and whether A element and etchants can produce stable products. The topochemical reaction shows a sigmoidal reaction curve, following typical self-accelerating reaction kinetics and the reaction activation energy is determined to be 60 kJ/mol. Reaction between Al atoms and hydrofluoric acid solution in the confined interlayer space between Ti_3C_2 layers is the rate-limiting step. Reaction energy derived from thermodynamics is a convenient descriptor of etching possibility with remarkable robustness. This descriptor can not only rationalize most of the experimental results in the literature and but also predict potential etchants efficiently. The results obtained in the present study are of reference and guiding significance to the rational design and topochemical transformation of layered materials into MXenes and other 2D materials.

Methods

Synthesis of Porous Ti_3AlC_2 Monolith. The porous Ti_3AlC_2 monolith (porosity, ~40%) used in this work was prepared in the authors' laboratory by the solid-liquid reaction synthesis method.⁴² The synthesis procedure adopted is in consistent with the earlier work.⁴³ The prepared porous monolith is phase-pure as determined by X-ray diffraction (XRD) examination.

Real-Time Gas Evolution Monitoring. Ti_3AlC_2 and HF acid aqueous solution react in the *reactor I* as the diagram (see Supplementary Fig. 14). *Reactor I* using the cork processed by PTFE rod and body of bottle made of PET, has been proven good air-tightness during experiments. The *Reactor I* needs to react in constant temperature, so it is put in a *water bath 5*. The generated gas of reaction passes through a Teflon tube into a filter to remove HF volatilized from *Reactor I*. *HF filter II* is equipped with the concentration of 1mol/L in the aqueous solution of NaOH. While the filtered gas is discharged into the *transparent gas collecting bottle III*, the water of the bottle is discharged in the *liquid collector IV*. The *liquid collector IV* has a very small opening to prevent the liquid from volatilization during the long time test. In order to ensure that the gas pressure above the water in *gas collecting bottle III* is kept at a pressure, the *gas collecting bottle III* is arranged on the platform of *Automatic elevator4*. When the laser is block by the float and laser receiver cannot receive laser, optical inductive switch is disconnected and elevator do not move. While the liquid level of the *gas collecting bottle IV* drops, the laser reaches the laser receiver through the transparent *gas collecting bottle III*, and optical inductive switch is connected, and the platform of *Automatic elevator4* is lift. After slightly descending, the laser is on the surface of the float block again, and elevator stop downward movement at the same time. *Automatic elevator4* always ensures the liquid level in *gas collecting bottle III* is lower than that of the liquid outlet for a fixed small distance we set before the experiment. By the means, the gas above the liquid pressure keeps a standard atmospheric pressure and the discharge volume of water and the molar amount of the gas have a linear relationship. *Gas collecting bottle III* is placed in the *balance 3*, which can record the quality once every two seconds. Meanwhile, the data is input into the computer. Through this set of platform, we can accurately measure the time and the Ti_3AlC_2 and HF acid aqueous solution reaction gas production curve. In every experiment, we use three pieces of samples, which size is about $2\text{ mm} \times 8\text{ mm} \times 15\text{ mm}$ and get the curve about gas production and time.

DFT Computation. The density functional theory (DFT) computations were performed by using the plane-wave technique as implemented in the Vienna ab initio simulation package (VASP).⁴⁴ The ion–electron interaction is described with the projector augmented wave (PAW) method.⁴⁵ A 500 eV cutoff was used for the plane-wave basis set. The exchange correlation energy is described by the functional of Perdew, Burke, and Ernzerhof (PBE).⁴⁶ The geometry optimizations were performed by using the conjugated gradient method, and the convergence threshold was set to be 10^{-4} eV in energy and 0.1 eV/Å in force. The Brillouin zone was represented by Monkhorst–Pack special k-point mesh of $5 \times 5 \times 1$ for geometry optimizations.⁴⁷ To investigate the splitting of H₂O on the Ti₃C₂ monolayers, three kinds of supercells was considered. A $3 \times 3 \times 1$, a $\sqrt{3} \times \sqrt{3} \times 1$ and a $1 \times 1 \times 1$ supercell with one adsorbed H₂O were used, and the PBE-D method, which introduces dispersion interactions by using an empirical potential of the form C_6R , was adopted.⁴⁸ Furthermore, the climbing-image nudged elastic band (CI-NEB) method implemented in VASP was used to determine the diffusion energy barrier and the minimum energy pathways for splitting of H₂O on the Ti₃C₂ surfaces.^{49, 50} This method involves optimizing a chain of images that connect the initial and final state. Each image is allowed to move only in the direction perpendicular to the hyper tangent. Hence, the energy is minimized in all directions except for the reaction path.

Data Availability

The authors declare that the data supporting the findings of this study are available within the paper and its supplementary information files. All of the other data are available from the corresponding author upon reasonable request.

Code Availability

The computational codes used in this work are available from the corresponding author on reasonable request.

Acknowledgements

This work was financially supported by the National Natural Science Foundation of China (No. 51902218 and 51972310). We would like to thank Dr Hui Zhang and Professor Xiaogang Yang for helpful discussion about the reaction mechanism. Part of this work was carried out at Guangzhou Computing Center of China, and the calculations were performed on Tianhe-2.

Competing interests

The authors declare no competing interests.

Supplementary Information

Supplementary Information. The online version contains supplementary material available at <https://doi.org/>.

Correspondence and requests for materials should be addressed to X.W.

References

1. Xiao X., Wang H., Urbankowski P. & Gogotsi Y. Topochemical synthesis of 2D materials. *Chem. Soc. Rev.* **47**, 8744-8765 (2018).
2. VahidMohammadi A., Rosen J. & Gogotsi Y. The world of two-dimensional carbides and nitrides (MXenes). *Science* **372**, eabf1581 (2021).
3. Alameda L. T., Moradifar P., Metzger Z. P., Alem N. & Schaak R. E. Topochemical deintercalation of Al from MoAlB: stepwise etching pathway, layered intergrowth structures, and two-dimensional MBene. *J. Am. Chem. Soc.* **140**, 8833-8840 (2018).
4. Wang J., *et al.* Discovery of hexagonal ternary phase Ti_2InB_2 and its evolution to layered boride TiB. *Nat. Commun.* **10**, 2284 (2019).
5. Bhaskar G., *et al.* Topochemical deintercalation of Li from layered LiNiB: toward 2D MBene. *J. Am. Chem. Soc.* **143**, 4213-4223 (2021).
6. Okamoto H., Sugiyama Y. & Nakano H. Synthesis and modification of silicon nanosheets and other silicon nanomaterials. *Chem. Eur. J.* **17**, 9864-9887 (2011).

7. Nakano H., *et al.* Soft synthesis of single-crystal silicon monolayer sheets. *Angew. Chem. Int. Ed.* **45**, 6303-6306 (2006).
8. Du Z., *et al.* Conversion of non-van der Waals solids to 2D transition-metal chalcogenides. *Nature* **577**, 492-496 (2020).
9. Ghidui M., Lukatskaya M. R., Zhao M. Q., Gogotsi Y. & Barsoum M. W. Conductive two-dimensional titanium carbide 'clay' with high volumetric capacitance. *Nature* **516**, 78-81 (2014).
10. Xia Y., *et al.* Thickness-independent capacitance of vertically aligned liquid-crystalline MXenes. *Nature* **557**, 409-412 (2018).
11. Li Z., *et al.* Reactive metal-support interactions at moderate temperature in two-dimensional niobium-carbide-supported platinum catalysts. *Nature Catalysis* **1**, 349-355 (2018).
12. Shahzad F., *et al.* Electromagnetic interference shielding with 2D transition metal carbides (MXenes). *Science* **353**, 1137-1140 (2016).
13. Naguib M., *et al.* Two-dimensional nanocrystals produced by exfoliation of Ti_3AlC_2 . *Adv. Mater.* **23**, 4248-4253 (2011).
14. Mashtalir O., *et al.* Intercalation and delamination of layered carbides and carbonitrides. *Nat. Commun.* **4**, 1716 (2013).
15. Alhabeb M., *et al.* Guidelines for synthesis and processing of two-dimensional titanium carbide ($\text{Ti}_3\text{C}_2\text{T}_x$ MXene). *Chem. Mater.* **29**, 7633-7644 (2017).
16. Natu V., *et al.* 2D $\text{Ti}_3\text{C}_2\text{T}_z$ MXene synthesized by water-free etching of Ti_3AlC_2 in polar organic solvents. *Chem* **6**, 616-630 (2020).
17. Xuan J., *et al.* Organic-base-driven intercalation and delamination for the production of functionalized titanium carbide nanosheets with superior photothermal therapeutic performance. *Angew. Chem. Int. Ed.* **55**, 14569-14574 (2016).
18. Yang S., *et al.* Fluoride-free synthesis of two-dimensional titanium carbide (MXene) using a binary aqueous system. *Angew. Chem. Int. Ed.* **57**, 15491-15495 (2018).

19. Yu X., *et al.* Fluorine-free preparation of titanium carbide MXene quantum dots with high near-infrared photothermal performances for cancer therapy. *Nanoscale* **9**, 17859-17864 (2017).
20. Li M., *et al.* Element replacement approach by reaction with Lewis acidic molten salts to synthesize nanolaminated MAX phases and MXenes. *J. Am. Chem. Soc.* **141**, 4730-4737 (2019).
21. Li Y., *et al.* A general Lewis acidic etching route for preparing MXenes with enhanced electrochemical performance in non-aqueous electrolyte. *Nat. Mater.* **19**, 894-899 (2020).
22. Wang C., *et al.* HCl-Based hydrothermal etching strategy toward fluoride-free MXenes. *Adv. Mater.* **33**, e2101015 (2021).
23. Alhabeb M., *et al.* Selective etching of silicon from Ti_3SiC_2 (MAX) to obtain 2D titanium carbide (MXene). *Angew. Chem. Int. Ed.* **130**, 5542-5546 (2018).
24. Kamysbayev V., *et al.* Covalent surface modifications and superconductivity of two-dimensional metal carbide MXenes. *Science* **369**, 979 (2020).
25. Hu T., *et al.* Chemical origin of termination-functionalized MXenes: $\text{Ti}_3\text{C}_2\text{T}_2$ as a case study. *J. Phys. Chem. C* **121**, 19254-19261 (2017).
26. Geng F., *et al.* Unusually stable ~100-fold reversible and instantaneous swelling of inorganic layered materials. *Nat. Commun.* **4**, 1632 (2013).
27. Jain A., *et al.* Commentary: The materials project: A materials genome approach to accelerating materials innovation. *APL Mater.* **1**, 011002 (2013).
28. Wang J., Liu B., Wang J. & Zhou Y. Theoretical investigation of thermodynamic stability and mobility of the intrinsic point defects in Ti_3AC_2 (A = Si, Al). *Phys. Chem. Chem. Phys.* **17**, 8927-8934 (2015).
29. Mashtalir O., Naguib M., Dyatkin B., Gogotsi Y. & Barsoum M. W. Kinetics of aluminum extraction from Ti_3AlC_2 in hydrofluoric acid. *Mater. Chem. Phys.* **139**, 147-152 (2013).
30. Haque R, Reeves LW. A study of the HF_2^- ion by fluorine magnetic resonance. *J. Am. Chem. Soc.* **89**, 250-252 (1967).
31. Slater J. C. Atomic Radii in Crystals. *J. Chem. Phys.* **41**, 3199-3204 (1964).

32. Hu T., Hu M., Gao B., Li W. & Wang X. Screening surface structure of MXenes by high-throughput computation and vibrational spectroscopic confirmation. *J. Phys. Chem. C* **122**, 18501-18509 (2018).
33. Liu Q., *et al.* Quantifying the nucleation and growth kinetics of microwave nanochemistry enabled by in situ high-energy X-ray scattering. *Nano Lett.* **16**, 715-720 (2016).
34. Zaikovskii V. I., Plyasova L. M., Ziborov A. V., Prudnikova O. Y. & Yur'eva T. M. The thermal decomposition of zinc hydroxocarbonate. *J. Struct. Chem.* **31**, 692-697 (1991).
35. Wang Y., Peng H. C., Liu J., Huang C. Z. & Xia Y. Use of reduction rate as a quantitative knob for controlling the twin structure and shape of palladium nanocrystals. *Nano Lett.* **15**, 1445-1450 (2015).
36. Pang S. Y., *et al.* Universal strategy for HF-free facile and rapid synthesis of two-dimensional MXenes as multifunctional energy materials. *J. Am. Chem. Soc.* **141**, 9610-9616 (2019).
37. Khazaei M., *et al.* Insights into exfoliation possibility of MAX phases to MXenes. *Phys. Chem. Chem. Phys.* **20**, 8579-8592 (2018).
38. Anasori B., Lukatskaya M. R. & Gogotsi Y. 2D metal carbides and nitrides (MXenes) for energy storage. *Nat. Rev. Mater.* **2**, 16098 (2017).
39. Sun W., *et al.* Electrochemical etching of Ti_2AlC to Ti_2CT_x (MXene) in low-concentration hydrochloric acid solution. *J. Mater. Chem. A* **5**, 21663-21668 (2017).
40. Wang X., *et al.* A new etching environment (FeF_3/HCl) for the synthesis of two-dimensional titanium carbide MXenes: a route towards selective reactivity vs. water. *J Mater Chem A* **5**, 22012-22023 (2017).
41. Zhao M. Q., *et al.* Synthesis of carbon/sulfur nanolaminates by electrochemical extraction of titanium from Ti_2SC . *Angew. Chem. Int. Ed.* **127**, 4892-4896 (2015).
42. Wang X. H. & Zhou Y. C. Solid-liquid reaction synthesis of layered machinable Ti_3AlC_2 ceramic. *J. Mater. Chem.* **12**, 455-460 (2002).

43. Hu M. M., *et al.* Self-assembled $\text{Ti}_3\text{C}_2\text{T}_x$ MXene film with high gravimetric capacitance. *Chem. Commun.* **51**, 13531-13533 (2015).
44. Kresse G. & Furthmüller J. Efficient iterative schemes for ab initio total-energy calculations using a plane-wave basis set. *Phys. Rev. B* **54**, 11169-11186 (1996).
45. Blöchl P. E. Projector augmented-wave method. *Phys. Rev. B* **50**, 17953-17979 (1994).
46. Perdew J. P., Burke K. & Ernzerhof M. Generalized gradient approximation made simple. *Phys. Rev. Lett.* **77**, 3865-3868 (1996).
47. Monkhorst H. J. & Pack J. D. Special points for Brillouin-zone integrations. *Phys. Rev. B* **13**, 5188-5192 (1976).
48. Grimme S. Semiempirical GGA-type density functional constructed with a long-range dispersion correction. *J. Comput. Chem.* **27**, 1787-1799 (2006).
49. Mills G., Jónsson H. & Schenter G. K. Reversible work transition state theory: application to dissociative adsorption of hydrogen. *Surf. Sci.* **324**, 305-337 (1995).
50. Henkelman G., Uberuaga B. P. & Jónsson H. A climbing image nudged elastic band method for finding saddle points and minimum energy paths. *J. Chem. Phys.* **113**, 9901-9904 (2000).

Electronic Supplementary Information for

Unveiling the spontaneous conversion of layered MAX phases to 2D MXenes

Author Information

Tao Hu^{1,2†}, Shihao Zhu^{1†}, Zhaojin Li^{1,3}, Da Li¹, Hongyang Liu¹, Chao Zhang¹ & Xiaohui Wang^{1*}

Affiliations

¹Shenyang National Laboratory for Materials Science, Institute of Metal Research, Chinese Academy of Sciences, Shenyang, China

²Institute of Materials Science and Devices, College of Materials Science and Engineering, Suzhou University of Science and Technology, Suzhou, China

³College of Materials Science and Engineering, Hebei University of Science and Technology, Shijiazhuang, China

Supplementary summary

Supplementary Figures **S3**

Supplementary Tables **S16**

Etching reaction models **S18**

Part I: Supplementary Figures

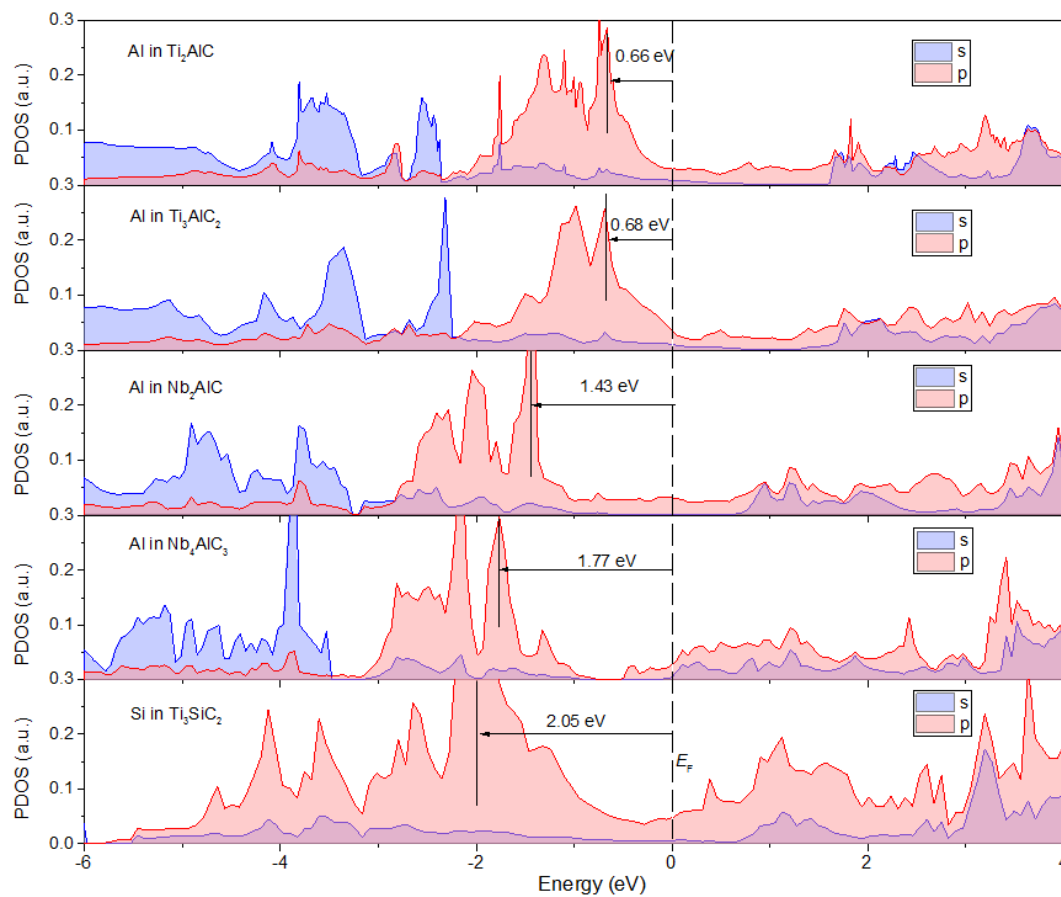


Fig. S1 Electronic structure of A atoms in Ti_2AlC , Ti_3AlC_2 , Nb_2AlC , Nb_4AlC_3 , and Ti_3SiC_2 . Pseudogap widths of A in MAX phases are indicated and generally in order of etching difficulty.

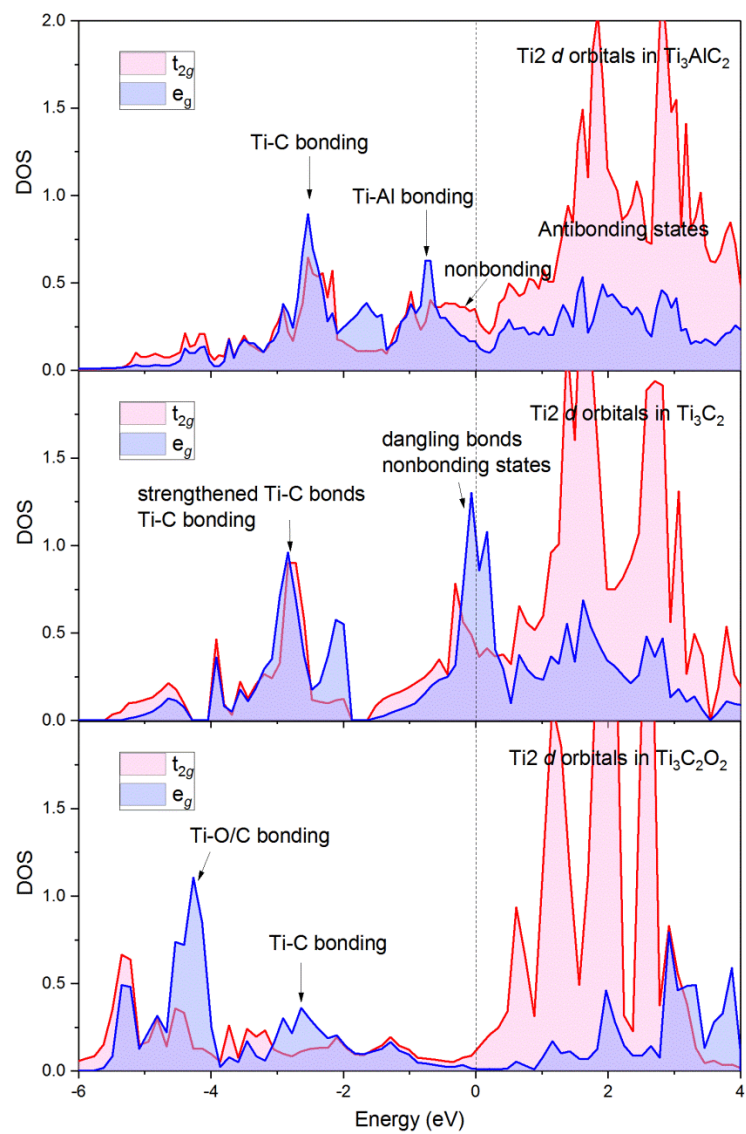


Fig. S2 Electronic structure evolution during the extraction of A atoms from Ti_3AC_2 MAX phases.

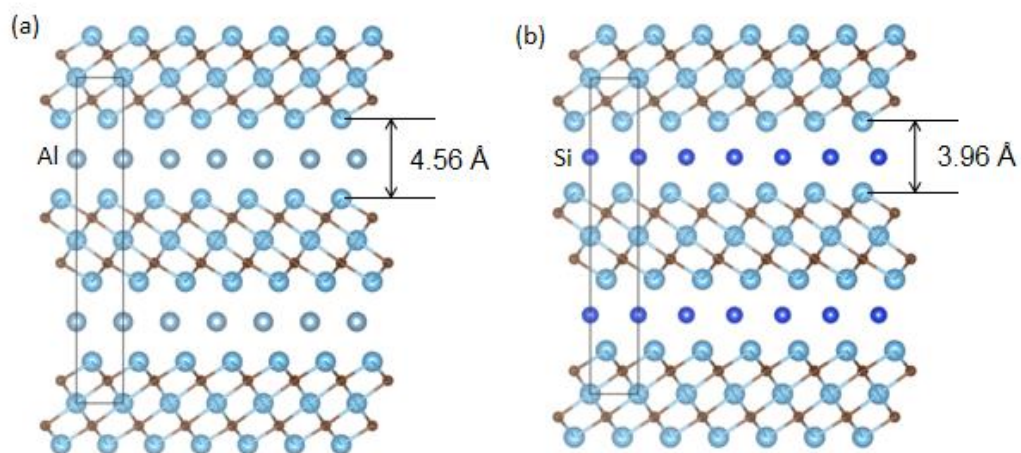


Fig. S3 Interlayer spacing in (a) Ti_3AlC_2 and (b) Ti_3SiC_2 .

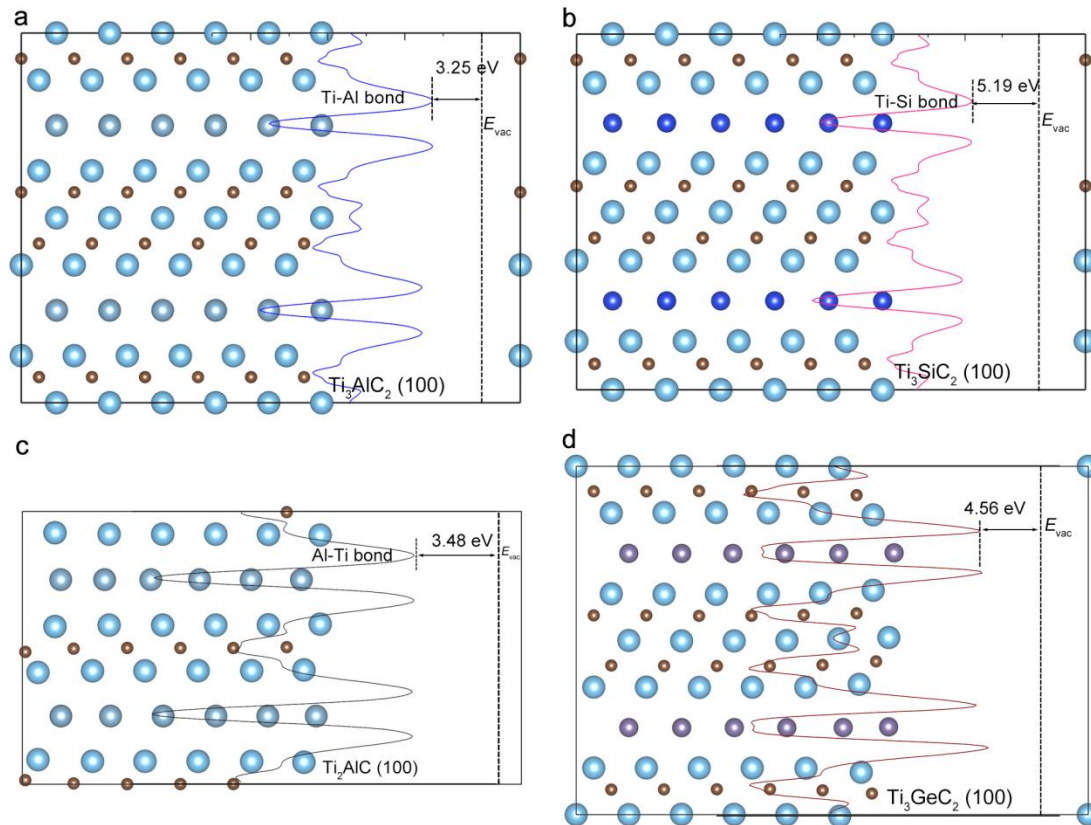


Fig. S4. Electrostatic potential at **a** $\text{Ti}_3\text{AlC}_2(100)$, **b** $\text{Ti}_3\text{SiC}_2(100)$, **c** $\text{Ti}_2\text{AlC}(100)$, **b** $\text{Ti}_3\text{GeC}_2(100)$. The potential at Ti-Al bond is higher and closer to E_{vac} , indicating the electrons around Ti-Al bonds are easier to be transferred.

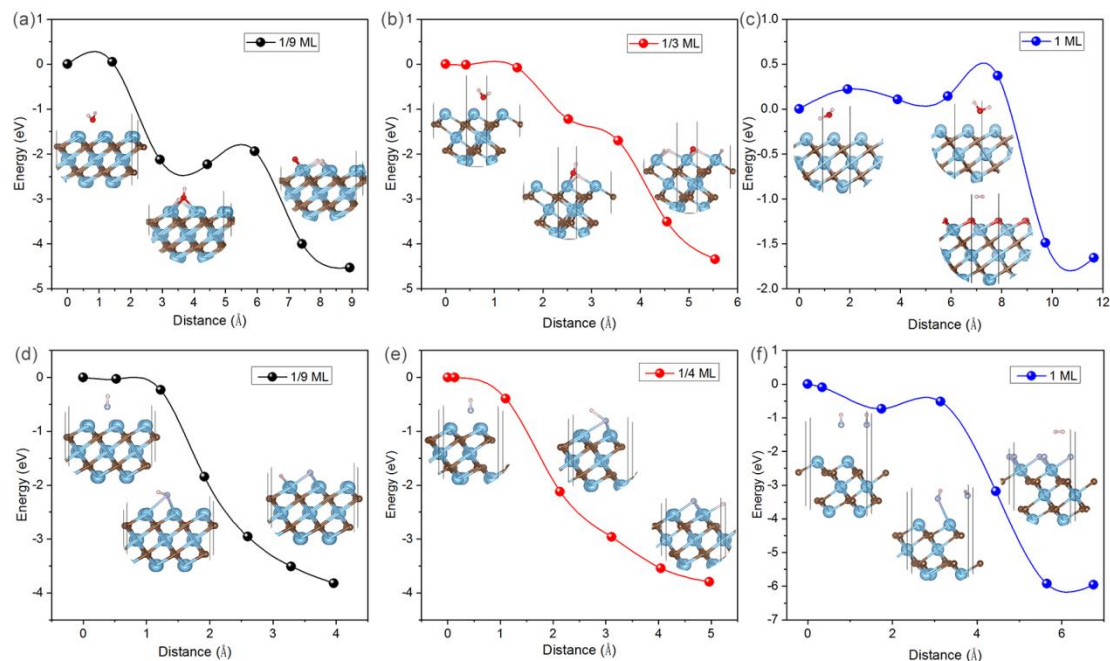


Fig. S5 Energy profiles of $\text{H}_2\text{O}/\text{HF}$ splitting on Ti_3C_2 monolayer. (a) low concentration, (b) middle concentration and (c) high concentration of H_2O molecules split on Ti_3C_2 monolayer. (d) low concentration, (e) middle concentration and (f) high concentration of HF molecules split on Ti_3C_2 monolayer. Note that low and middle concentration H_2O and HF split on Ti_3C_2 monolayer in terms of adsorbed O, F, and H. High concentration H_2O or HF result in O or F termination and H_2 gas.

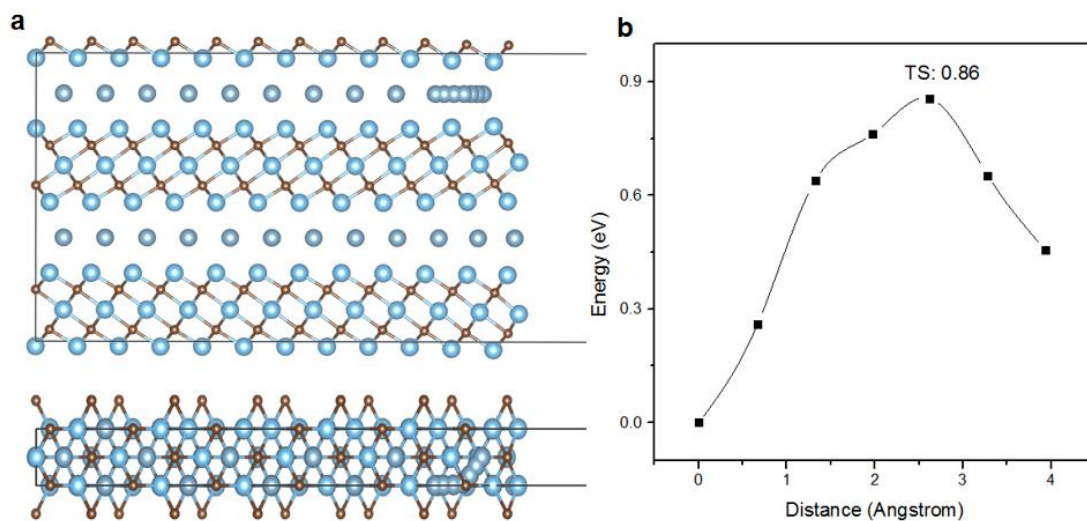


Fig. S6 The energy barrier of Al atom migration along the interlayer tunnel without termination.

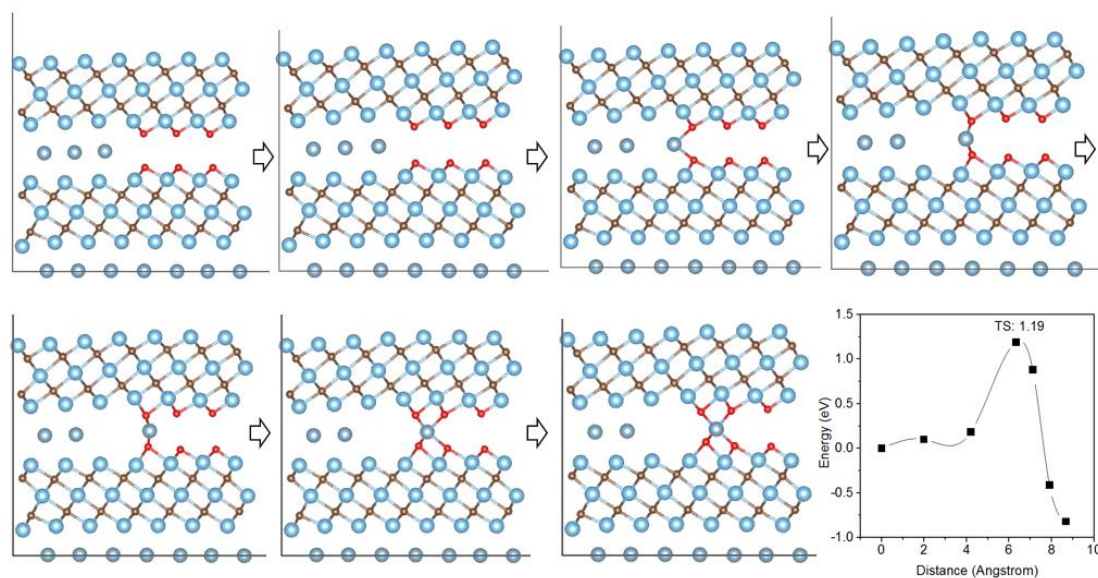


Fig. S7 The energy barrier of Al atom migration along the interlayer tunnel with O termination.

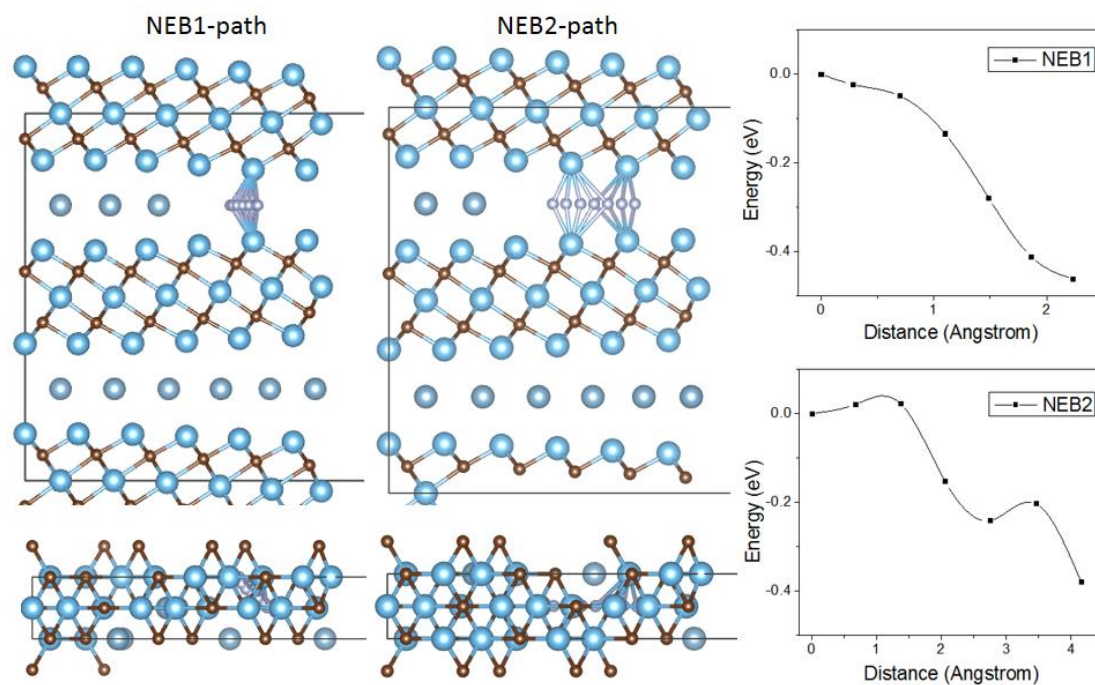


Fig. S8 The energy barriers of F^- ion migration along tunnel into the Ti_3AlC_2 interlayer. The unique penetrating ability of F^- is the key factor in the etching process.

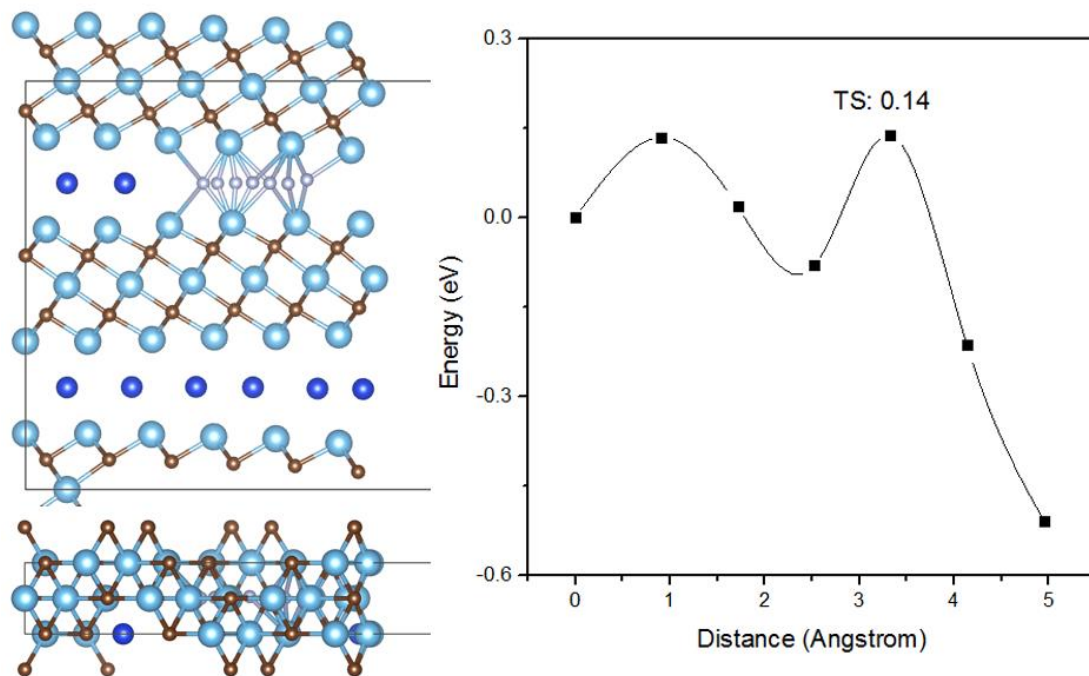


Fig. S9 The energy barriers of F⁻ ion migration along tunnel into the Ti₃SiC₂ interlayer. The unique penetrating ability of F⁻ is the key factor in the etching process.

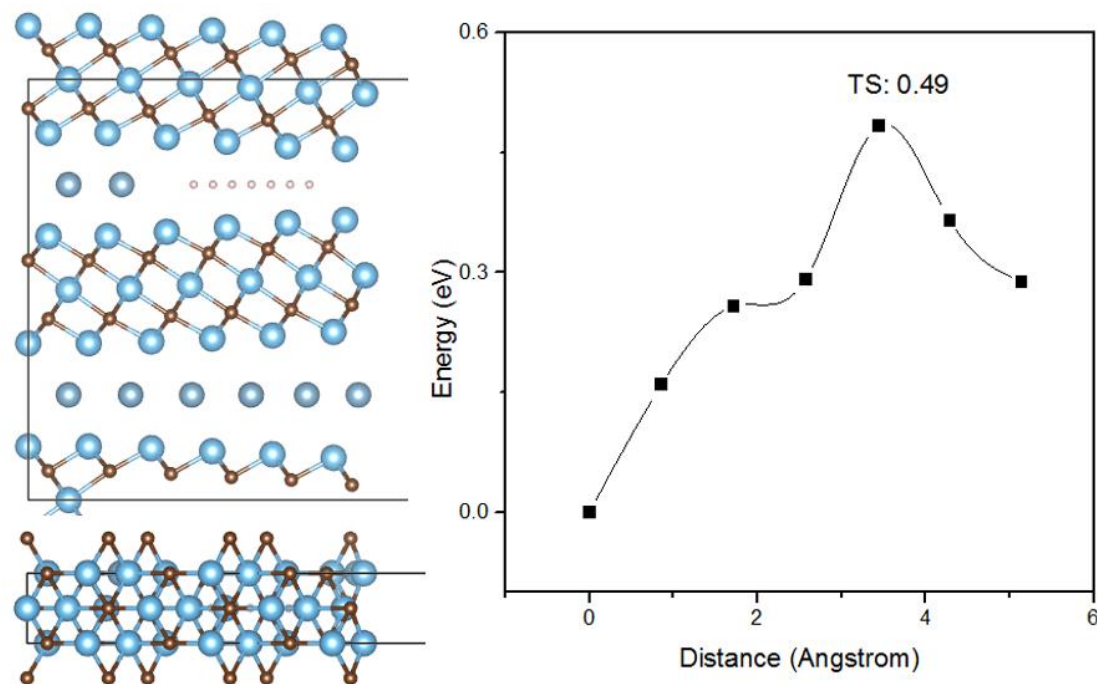


Fig. S10 The energy barriers of H⁺ ion migration along the interlayer tunnel into the interlayer.

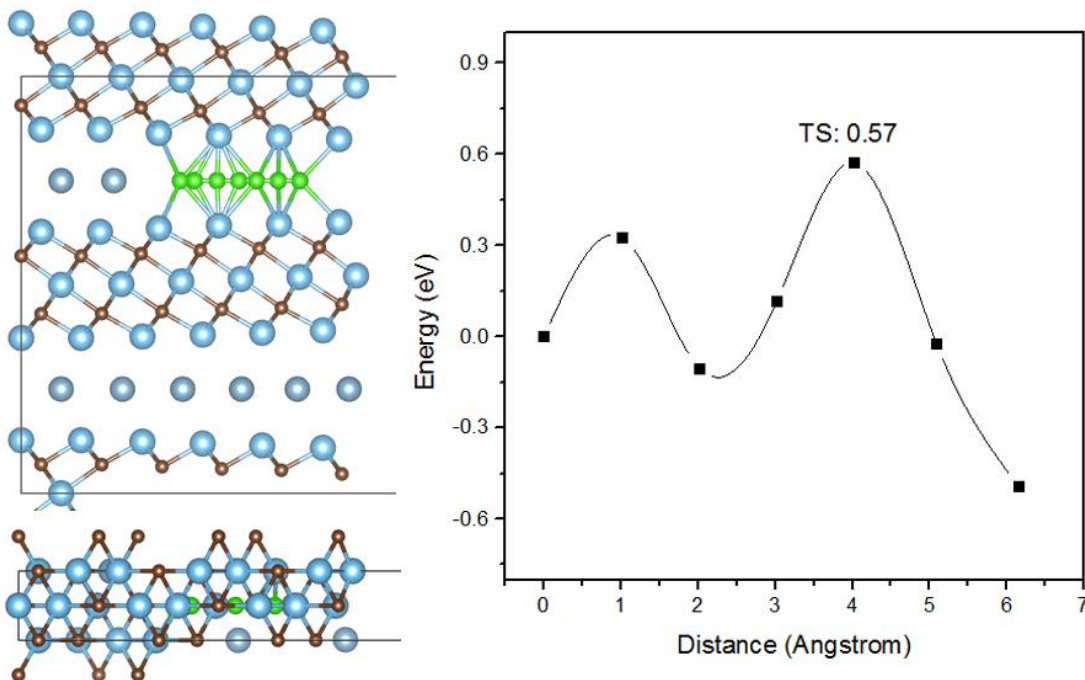


Fig. S11 The energy barriers of Cl^- ion migration along the tunnel into the interlayer.

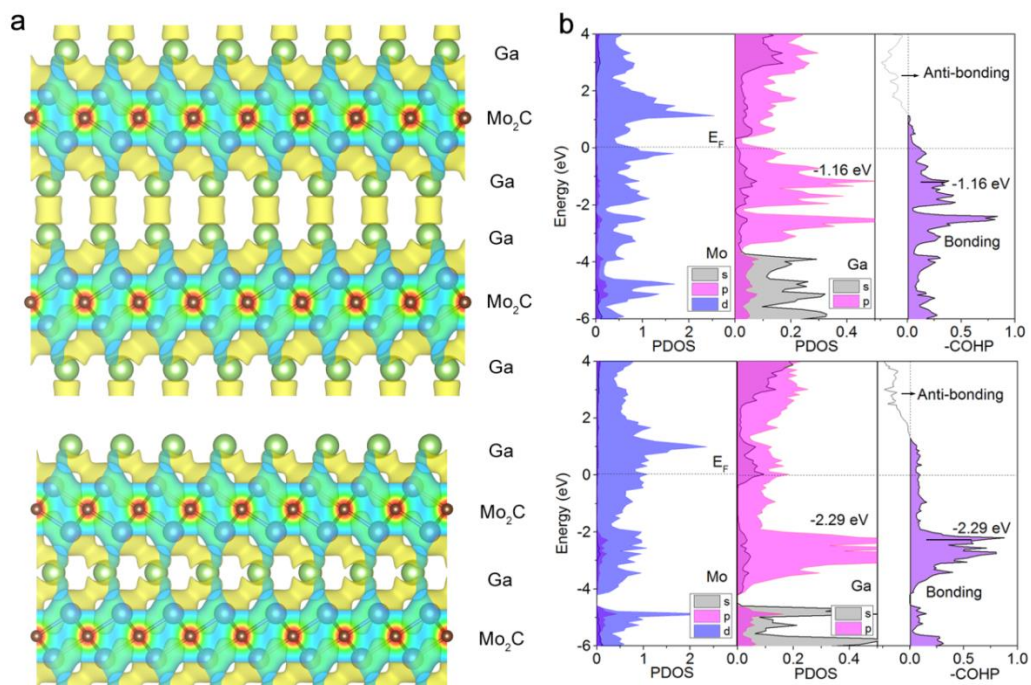


Fig. S12 Electronic structure of A atoms in $\text{Mo}_2\text{Ga}_2\text{C}$, and Mo_2GaC . $\text{Mo}_2\text{Ga}_2\text{C}$ with smaller pseudogaps has been successfully etched by hydrochloric acid while Mo_2GaC has not yet.

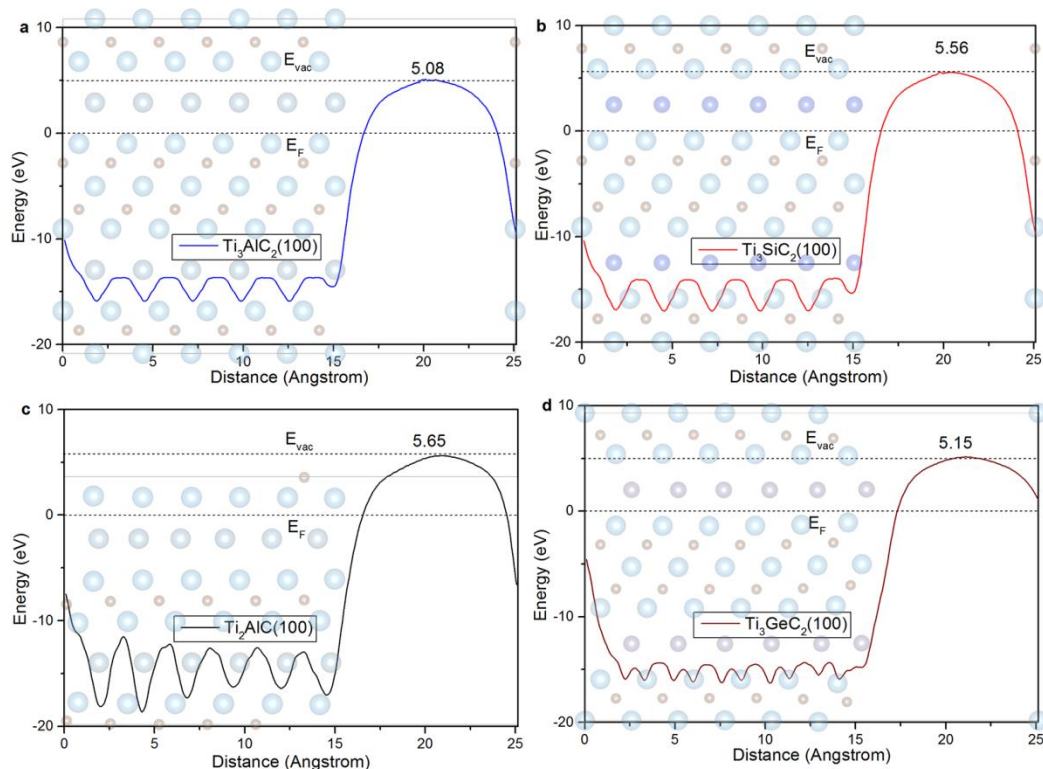


Fig. S13 Work functions of $Ti_3AlC_2(100)$ and $Ti_3SiC_2(100)$. The work function of $Ti_3AlC_2(100)$ is about 0.5 eV smaller than that of $Ti_3SiC_2(100)$. The trend is in agreement with earlier studies that corrosion behavior of metal can be correlated with work function. However, using work function as a descriptor of etching in MAX phases with anisotropic bonding character would be with caution. As the work function of a certain surface is the average of local potential, the more negative Al proportion would increase the calculated work function. For example, calculated work function of $Ti_2AlC(100)$ is 5.65 eV, which is even larger than that of $Ti_3SiC_2(100)$. Therefore, the bond-specific local potential is more meaningful for corrosion of materials with anisotropic bonding character.

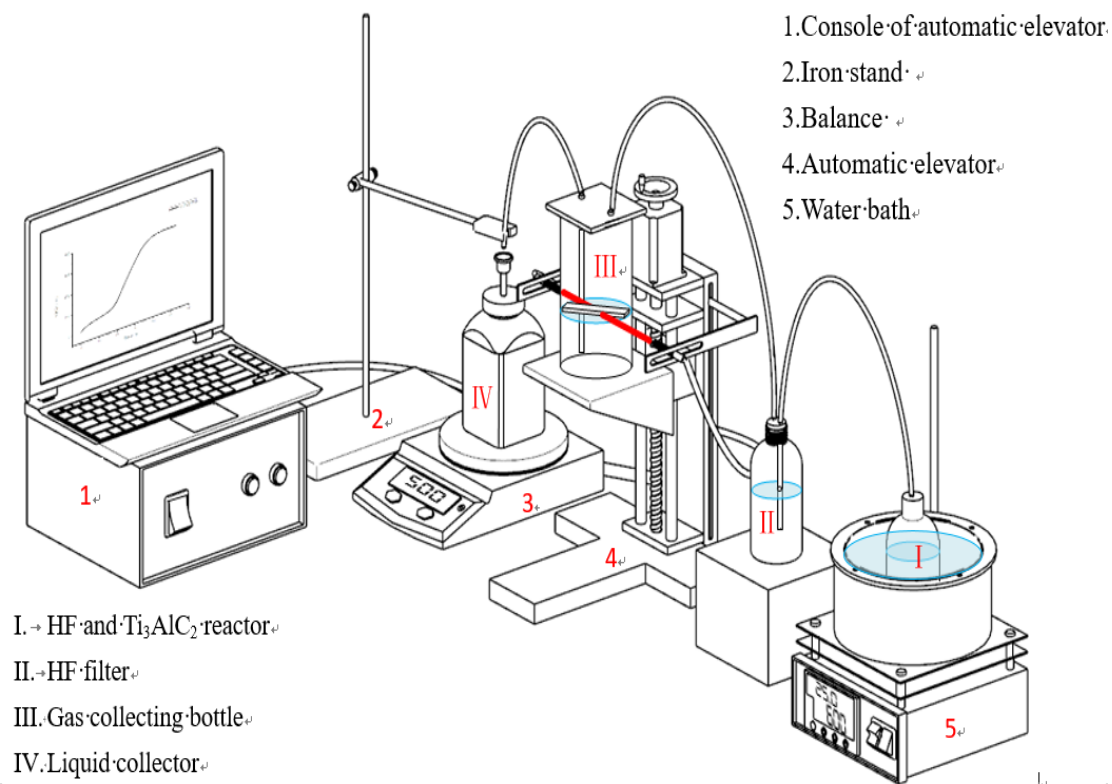


Fig. S14 Schematic illustration of the online gas evolution monitoring equipment.

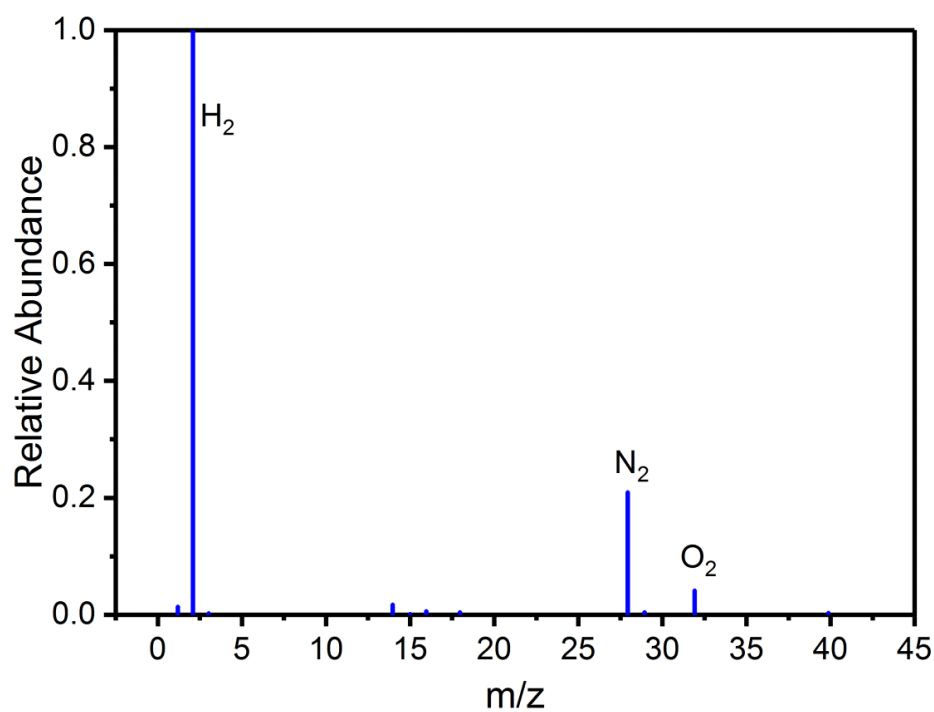


Fig. S15 Mass spectrum for the determination of released gases collected in the etching reaction.

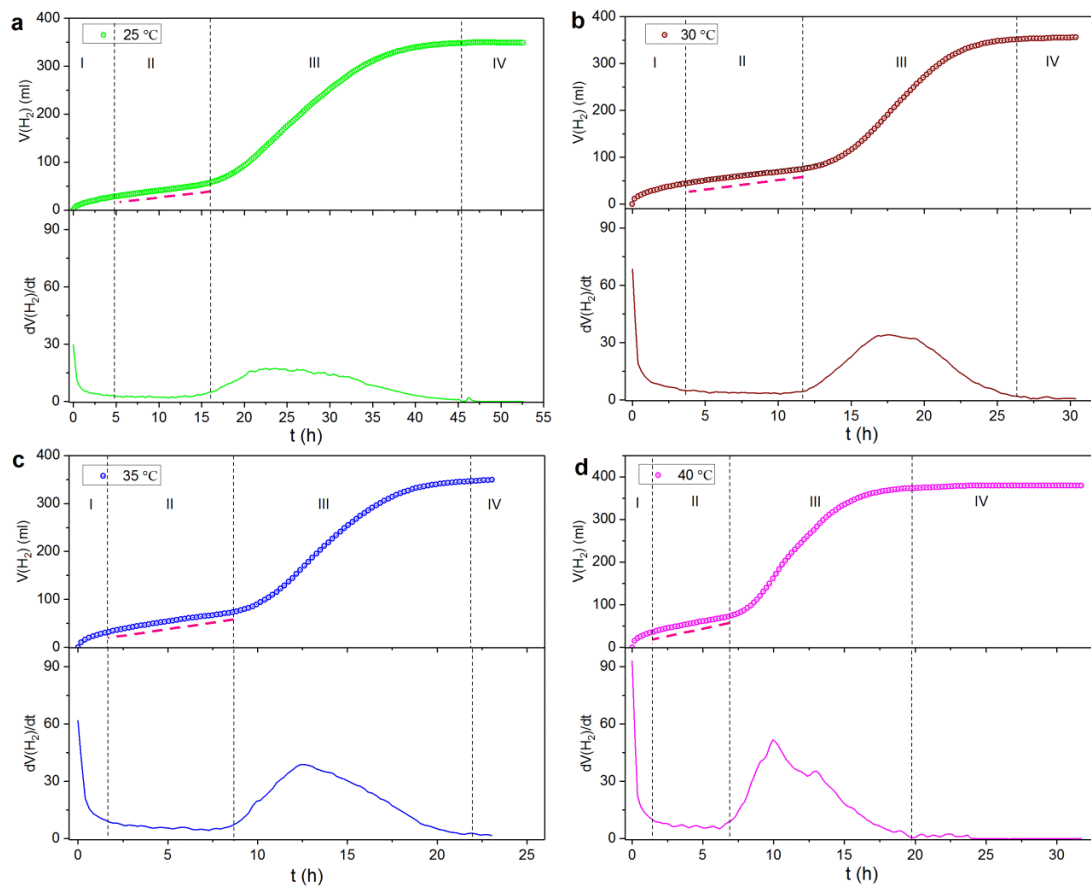


Fig. S16 Etching reactions of Ti_3AlC_2 MAX phase at different temperature can be divided into four stages. Online H_2 monitoring of hydrofluoric acid (40%) etching Ti_3AlC_2 and its derivative at **a** 25 °C, **b** 30 °C, **c** 35 °C, and **d** 40 °C.

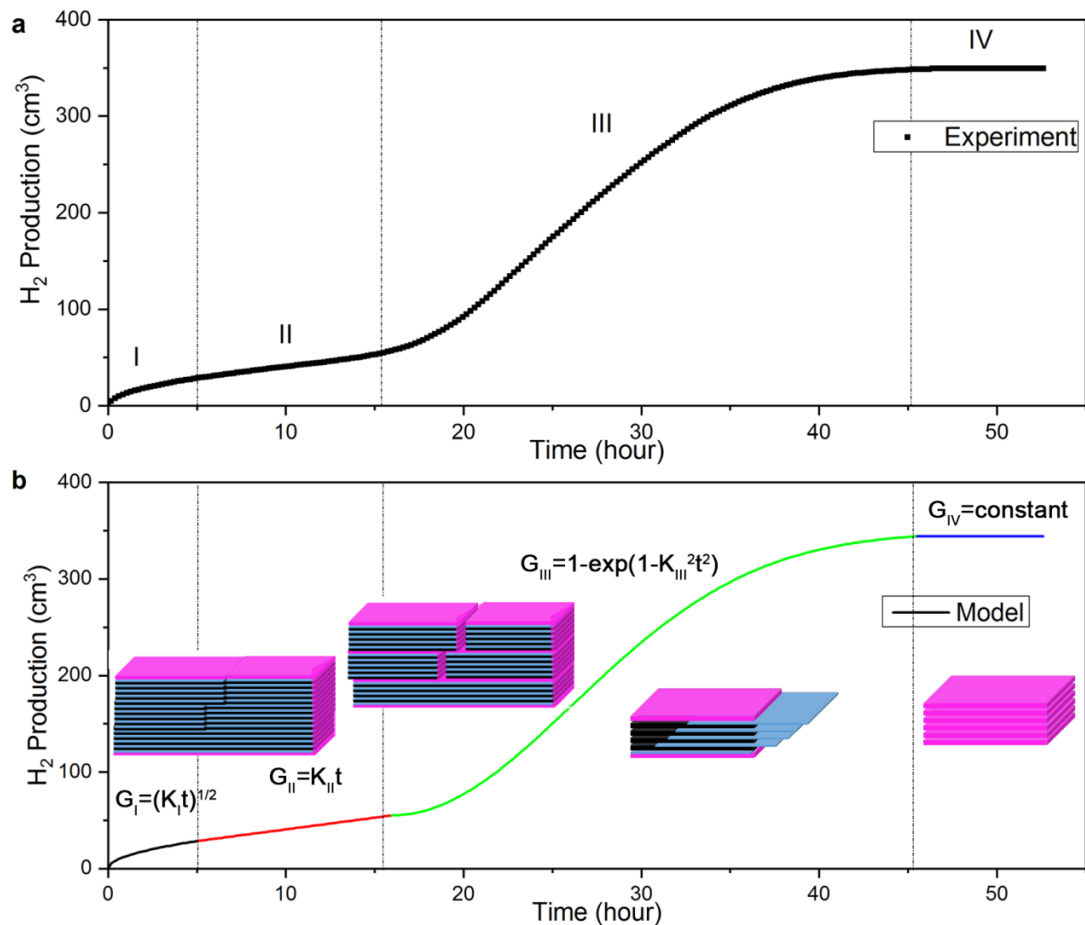


Fig. S17 Comparison of experimentally collected data and modeling results. a Experimentally collected gas evolution data of Ti₃AlC₂ emerging in 40% HF aqueous solution at 25°C. **b** Modeling results and schematic illustration of etching process of MAX phases. (I) Pre-etching process. (II) Induction period. (III) Accelerating period (burst etching). (IV) Completion of etching.

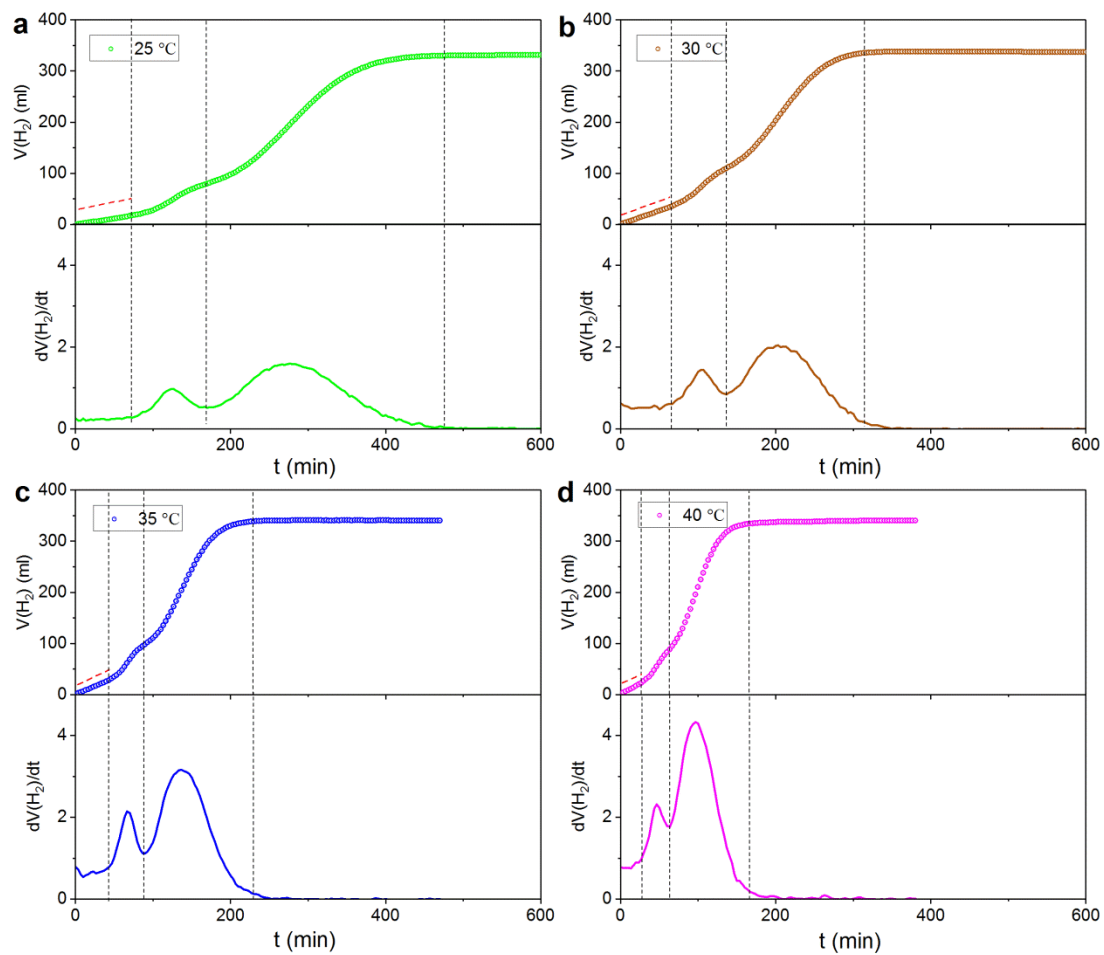


Fig. S18 Etching reactions of HF-treated Ti_3AlC_2 MAX phase at different temperature can be divided into four stages. Online H_2 monitoring of hydrofluoric acid (50%) etching HCl-treated Ti_3AlC_2 and its derivative at **a** 25 °C, **b** 30 °C, **c** 35 °C, **d** 40 °C.

Part II: Supplementary Tables

Table S1. Atomic radii¹ and ionic radii² of H, F, Cl, Al and Si

Atomic species	Atomic radius (pm)	Ionic radius (pm)
H	25	-4
F	50	128
Cl	100	181
Al	125	39
Si	110	26

Table S2. Reaction energies of MAX phases with HF

	M ₂ X				M ₃ X ₂		M ₄ X ₃		
A	Ti ₂ C	Nb ₂ C	V ₂ C	Mo ₂ C	Ti ₃ C ₂	Zr ₃ C ₂	Ti ₄ N ₃	Nb ₄ C ₃	Ta ₄ C ₃
Al	-7.85	-7.15	-7.43	-6.92	-8.04	-8.25	-7.25	-7.39	-7.34
Ga	1.39	1.73	1.38	1.56	1.23	1.16	1.76	1.54	1.47
Ga ₂	-3.54	-2.91	-3.18	-2.69	-3.62	-4.28	-3.13	-3.28	-3.12
In	1.70	1.84	1.03	1.47	1.53	1.92	1.57	1.78	1.50
Tl	6.88	6.70	5.83	6.09	6.69	7.28	6.40	6.60	6.16
Si	-4.23	-4.01	-4.36	-4.41	-4.48	-4.55	-4.48	-4.89	-4.93
Ge	4.79	4.66	4.09	4.12	8.65	4.79	4.35	3.91	3.62
Sn	2.35	2.07	1.21	1.69	6.57	2.86	1.50	1.56	0.96
Pb	7.97	7.55	6.75	6.98	7.74	8.71	6.76	7.07	6.34
P	4.77	5.21	4.27	3.30	4.34	5.28	4.29	4.28	4.21
As	10.38	10.49	9.46	8.92	9.96	10.89	9.57	9.48	9.14
S	18.84	17.30	16.49	15.00	18.31	19.44	17.34	16.39	15.78

Table S3. Reaction energies of MAX phases with HCl

	M ₂ X	M ₃ X ₂	M ₄ X ₃
--	------------------	-------------------------------	-------------------------------

A	Ti ₂ C	Nb ₂ C	V ₂ C	Mo ₂ C	Ti ₃ C ₂	Zr ₃ C ₂	Ti ₄ N ₃	Nb ₄ C ₃	Ta ₄ C ₃
Al	-1.40	-0.70	-0.98	-0.47	-1.59	-1.80	-0.80	-0.94	-0.89
Ga	2.28	2.62	2.27	2.45	2.12	2.05	2.65	2.43	2.36
Ga ₂	-1.76	-1.13	-1.40	-0.91	-1.84	-2.50	-1.35	-1.50	-1.34
In	2.46	2.59	1.78	2.22	2.28	2.67	2.33	2.53	2.25
Tl	4.49	4.32	3.45	3.71	4.31	4.90	4.01	4.22	3.77
Si	0.57	0.80	0.44	0.40	0.33	0.26	0.33	-0.09	-0.13
Ge	4.12	3.98	3.42	3.44	7.98	4.11	3.67	3.24	2.95
Sn	3.11	2.83	1.97	2.45	7.33	3.62	2.26	2.32	1.75
Pb	5.21	4.79	3.98	4.22	4.98	5.95	3.99	4.30	3.58
P	9.48	9.92	8.98	8.02	9.05	10.00	9.00	8.99	8.92
As	10.33	10.44	9.41	8.86	9.91	10.84	9.52	9.42	9.09
S	11.02	9.48	8.67	7.18	10.49	11.62	9.52	8.57	7.96

Part III: Etching reaction models

1. Reaction-controlled	3D	1.1 F -sphere $(1-G)^{-\frac{2}{3}} - 1 = \frac{8}{3} \pi K R_0^2 K t$
		1.2 n particles react simultaneously $(1-G)^{-\frac{2}{3}} = \frac{8}{3} \pi K R_0^2 \left[\frac{t^3}{3} - c_1 t^2 + (c_1^2 + c_2) t \right] + 1$
		1.3 F -constant $\ln(1-G) = -K F t$
	2D	1.4 F -round plate $(1-G)^{-\frac{1}{2}} - 1 = K' t$
		1.5 n layers react simultaneously $\frac{1}{\sqrt{1-G}} = \pi K R_0 \left[\frac{1}{3} t^3 - c_1 t^2 + (c_1^2 + c_2) t \right] + 1$
		1.6 F -constant $\ln(1-G) = -K F t$
2. Diffusion-controlled	3D	2.1 Jander's sphere model $[1 - (1-G)^{\frac{1}{3}}]^2 = \frac{K}{R_0^2} t$
		2.2 Ginsterlinger's sphere model $1 - \frac{2}{3} G - (1-G)^{\frac{2}{3}} = K' t$
		2.3 Ginsterlinger's cylinder model $\ln(1-G) \cdot (1-G) + G = \frac{4K'}{R_0^2} t$
	2D	2.4 Plate model $[1 - (1-G)^{\frac{1}{2}}]^2 = \left(\frac{K}{R_0}\right)^2 t$
		2.5 Round plate model $2(1-G)^{\frac{3}{2}} - 3(1-G) + 1 = K' t$
		2.6 Constant interface shift velocity $1 - (1-G)^{\frac{1}{2}} = K' t$

For solid state reactions encompassing diffusion and chemical reactions, the reaction rate of total reaction v , diffusion rate v_D , and chemical reaction rate v_R follow the relationship,

$$\frac{1}{v} = \frac{1}{v_R} + \frac{1}{v_D}$$

The total reaction rate is determined by the slowest process. The rate of reaction and diffusion are expressed as the following equations respectively:

$$v_R = k_c$$

$$v_D = D \frac{dc}{dx} = D \frac{c_0 - c}{\delta}$$

When the process reaches an equilibrium,

$$v = v_R = v_D$$

$$k_c = D \frac{c_0 - c}{\delta}$$

The etching of layered compounds is the reaction between solid and liquid, belongs to the general solid state reaction. Suppose that supplying the etchants, HF and H₂O in great excess relative to the precursor to ensure that the concentration of the etchant would mainly remain as a constant throughout the reaction. Under such assumption, the rate can be described as following:

$$rate = \frac{d[MXene]}{dt} = k[MX][etchant] = k[MX]$$

the reaction rate $\frac{dG}{dt}$ is dependent on the unreacted MAX phases (1-G).

$$\frac{dG}{dt} = KF(1-G)^n$$

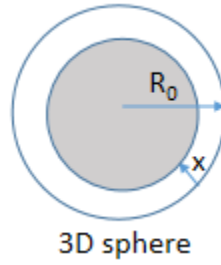
1. Reaction-controlled

$$\frac{dG}{dt} = KF(1-G)^n \quad (S1)$$

G is the reacted part, t is the reaction time, k is the reaction rate constant, F is the reaction interface, n is the reaction order. Assuming the reaction happens at the unreacted part ($1-G$), while the reacted part (G) does not contribute to the reaction rate. Considering only the first-order reaction ($n=1$), then

$$\frac{dG}{dt} = KF(1-G) \quad (\text{S2})$$

1.1 F-sphere

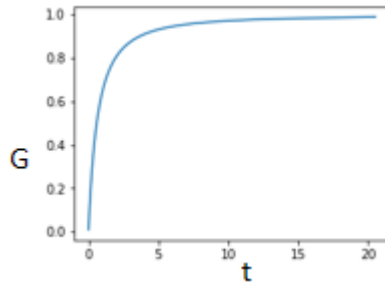


$$G = \frac{V}{V_0} = \frac{\frac{4}{3}\pi R_0^3 - \frac{4}{3}\pi (R_0 - x)^3}{\frac{4}{3}\pi R_0^3} = \frac{R_0^3 - (R_0 - x)^3}{R_0^3}$$

$$F = 4\pi(R_0 - x)^2 = 4\pi R_0^2 (1-G)^{\frac{2}{3}}$$

$$\frac{dG}{dt} = KF(1-G) = 4\pi R_0^2 K(1-G)^{\frac{5}{3}}$$

$$(1-G)^{\frac{2}{3}} - 1 = 4\pi R_0^2 Kt$$



1.2 Considering one polycrystalline Ti_3AlC_2 particle divided into n nanocrystal particle.

$$G = \frac{V}{V_0} = \frac{[\frac{4}{3}\pi R_n^3 - \frac{4}{3}\pi(R_n - x)^3] \cdot n}{\frac{4}{3}\pi R_n^3 \cdot n} = \frac{R_n^3 - (R_n - x)^3}{R_n^3} = 1 - (1 - \frac{x}{R_n})^3$$

$$F = 4\pi(R_n - x)^2 \cdot n = n \cdot 4\pi R_n^2 (1 - \frac{x}{R_n})^2 = 4\pi n R_n^2 (1 - G)^{\frac{2}{3}}$$

For first order reaction,

$$\frac{dG}{dt} = KF(1 - G) = K \cdot 4\pi n R_n^2 (1 - G)^{\frac{2}{3}} \cdot (1 - G) = K \cdot 4\pi n R_n^2 (1 - G)^{\frac{5}{3}}$$

$$n \cdot \frac{4}{3}\pi R_n^3 = \frac{4}{3}\pi R_0^3$$

$$R_n = n^{-\frac{1}{3}} R_0$$

$$\frac{dG}{dt} = K \cdot 4\pi n R_n^2 (1 - G)^{\frac{5}{3}} = K \cdot 4\pi n \cdot n^{-\frac{2}{3}} R_0^2 (1 - G)^{\frac{5}{3}} = 4\pi K n^{\frac{1}{3}} R_0^2 (1 - G)^{\frac{5}{3}}$$

(1) In the situation that the particle number is the function of time, and given by $n = ct$

$$\frac{dG}{dt} = 4\pi K n^{\frac{1}{3}} R_0^2 (1 - G)^{\frac{5}{3}} = 4\pi K c^{\frac{1}{3}} t^{\frac{1}{3}} R_0^2 (1 - G)^{\frac{5}{3}}$$

$$(1 - G)^{-\frac{5}{3}} dG = 4\pi K c^{\frac{1}{3}} R_0^2 t^{\frac{1}{3}} dt$$

$$\frac{3}{2}(1 - G)^{-\frac{2}{3}} = 4\pi K c^{\frac{1}{3}} R_0^2 t^{\frac{4}{3}} \cdot \frac{3}{4} + C$$

$$t = 0, G = 0$$

$$C = \frac{3}{2}$$

$$(1 - G)^{-\frac{2}{3}} = 2\pi K c^{\frac{1}{3}} R_0^2 t^{\frac{4}{3}} + 1$$

(2) In the situation that the particle number is given by

$$n = (t - c_1)^2 + c_2$$

$$\frac{dG}{dt} = 4\pi K [(t - c_1)^2 + c_2] R_0^2 (1 - G)^{\frac{5}{3}}$$

$$(1 - G)^{-\frac{5}{3}} dG = 4\pi K R_0^2 [(t - c_1)^2 + c_2] dt$$

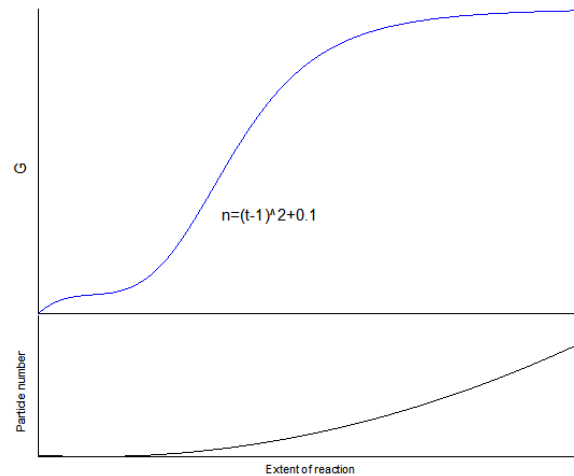
$$(1 - G)^{-\frac{2}{3}} = \frac{8}{3} \pi K R_0^2 \left[\frac{t^3}{3} - c_1 t^2 + (c_1^2 + c_2) t \right] + 1$$

$$G = 1 - \left\{ \frac{8}{3} \pi K R_0^2 \left[\frac{t^3}{3} - c_1 t^2 + (c_1^2 + c_2) t \right] + 1 \right\}^{-\frac{3}{2}}$$

$$c_1 = 1, c_2 = 0.1, \frac{8}{3} \pi K R_0^2 = 0.1$$

$$G = 1 - \left\{ 0.1 \left[\frac{t^3}{3} - t^2 + 1.1 t \right] + 1 \right\}^{-\frac{3}{2}}$$

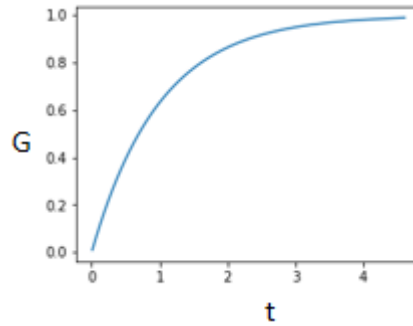
The G - t is plot as



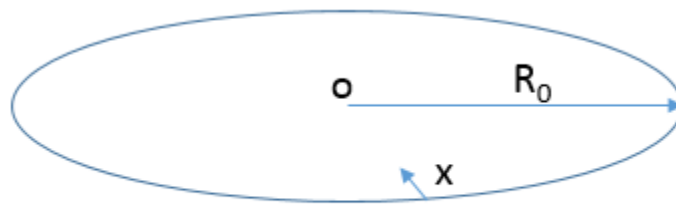
1.3 F -constant (3D)

$$\frac{dG}{dt} = KF(1 - G) = K'(1 - G)$$

$$-\ln(1 - G) = K't$$



1.4 F -round plate model:



2D reaction

$$G = 1 - \frac{S}{S_0} = 1 - \frac{\pi(R_0 - x)^2}{\pi R_0^2} = 1 - \frac{(R_0 - x)^2}{R_0^2}$$

$$F \text{ is a function of } G: F = 2\pi(R_0 - x) = 2\pi R_0(1 - G)^{\frac{1}{2}}$$

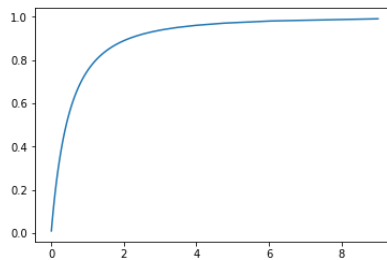
$$\frac{dG}{dt} = KF(1 - G) = 2\pi K R_0(1 - G)^{\frac{3}{2}}$$

$$2(1 - G)^{-\frac{1}{2}} = 2\pi K R_0 t + 2$$

$$2\pi K R_0 = K'$$

$$(1 - G)^{-\frac{1}{2}} - 1 = K' t$$

When $K' = 1$



1.5 n layers react at the same time

For 2D round plate model

$$G = 1 - \frac{S}{S_0} = 1 - \frac{\pi(R_0 - x)^2}{\pi R_0^2} = 1 - \frac{(R_0 - x)^2}{R_0^2}$$

F is a function of G : $F = 2\pi(R_0 - x) = 2\pi R_0(1 - G)^{\frac{1}{2}}$

For reactions of n layers are initiated at the same time,

$$\frac{dG}{dt} = nKF(1 - G) = 2\pi nKR_0(1 - G)^{\frac{3}{2}}$$

(1) For $n = ct$

$$(1 - G)^{\frac{3}{2}} dG = 2\pi KR_0 c t dt$$

$$2(1 - G)^{\frac{1}{2}} = \pi KR_0 c t^2 + 2$$

$$G = 1 - \frac{4}{(2 + \pi KR_0 c t^2)^2}$$

$$\frac{d^2 G}{dt^2} = \pi KR_0 c \frac{d}{dt} [t(1 - G)^{\frac{3}{2}}]$$

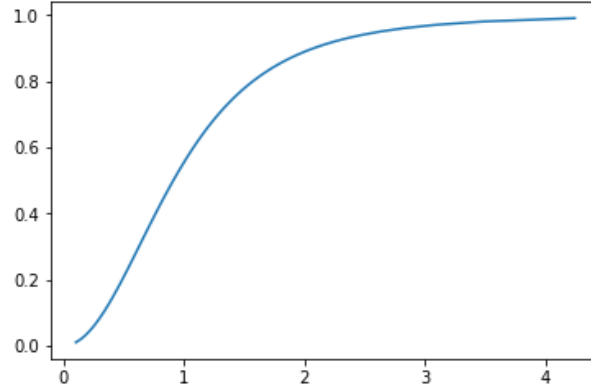
$$u = t, v = (1 - G)^{\frac{3}{2}}$$

$$(uv)' = u'v + uv' = (1 - G)^{\frac{3}{2}} - \frac{3}{2}(1 - G)^{\frac{1}{2}} t [2\pi KR_0 c t (1 - G)^{\frac{3}{2}}] = (1 - G)^{\frac{3}{2}} [1 - 3\pi KR_0 c (1 - G)^{\frac{1}{2}} t^2]$$

$$1 - 3\pi KR_0 c (1 - G)^{\frac{1}{2}} t^2 = 1 - 3(1 - G)^{\frac{1}{2}} \left(\frac{2}{\sqrt{1 - G}} - 2 \right) = 6\sqrt{1 - G} - 5$$

$$0 < G < 0.31, (uv)' > 0, \frac{d^2 G}{dt^2} > 0$$

$$0.31 < G < 1, (uv)' < 0, \frac{d^2 G}{dt^2} < 0$$



(2) For $n = (t - c_1)^2 + c_2$

$$\frac{dG}{dt} = n * 2\pi KR_0 (1-G)^{\frac{3}{2}} = 2\pi KR_0 [(t - c_1)^2 + c_2] (1-G)^{\frac{3}{2}}$$

$$\int (1-G)^{-\frac{3}{2}} dG = \int 2\pi KR_0 [(t - c_1)^2 + c_2] dt$$

$$2(1-G)^{-\frac{1}{2}} = 2\pi KR_0 \left[\frac{1}{3} t^3 - c_1 t^2 + (c_1^2 + c_2)t + c_3 \right]$$

$$t = 0, G = 0, c_3 = \frac{1}{2\pi KR_0}$$

$$\frac{1}{\sqrt{1-G}} = \pi KR_0 \left[\frac{1}{3} t^3 - c_1 t^2 + (c_1^2 + c_2)t \right] + 1$$

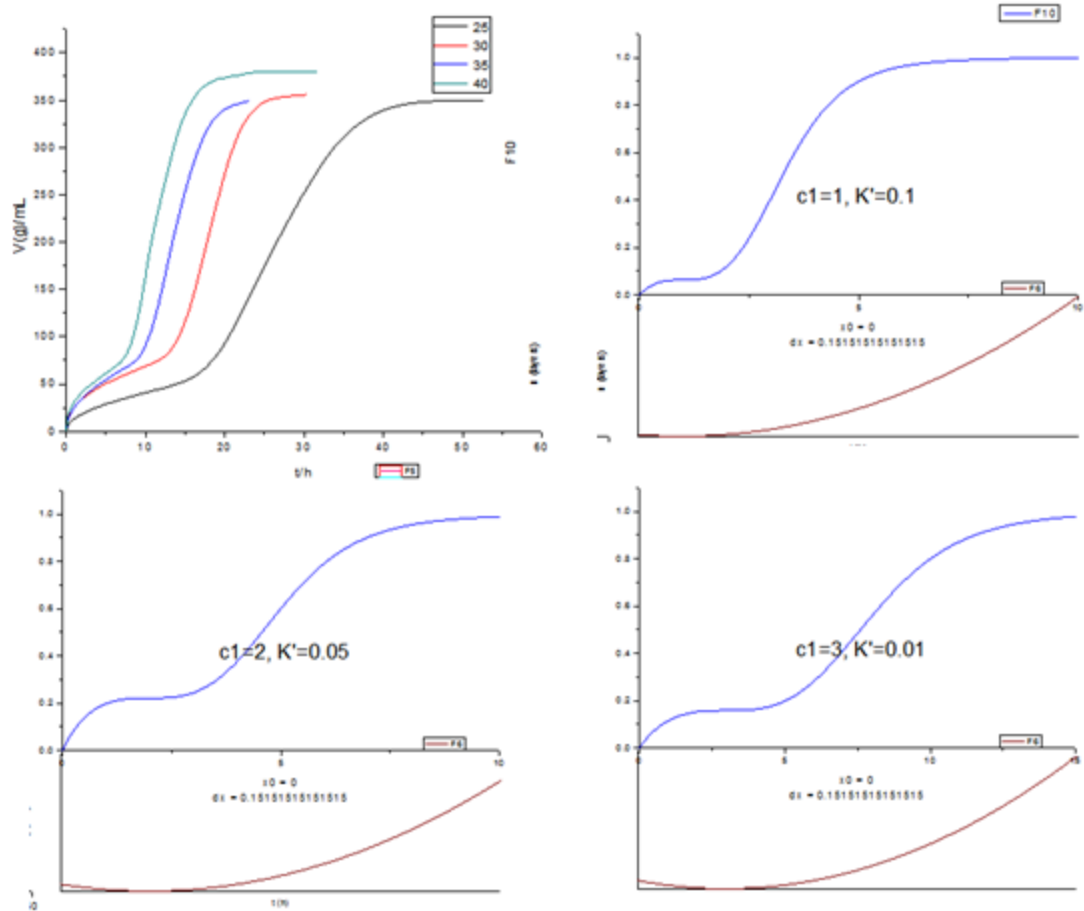
$$c_2 = 0, n = (t - c_1)^2$$

$$\frac{1}{\sqrt{1-G}} = \pi KR_0 \left[\frac{1}{3} t^3 - c_1 t^2 + c_1^2 t \right] + 1$$

$$G = 1 - \frac{1}{\left[\pi KR_0 \left(\frac{1}{3} t^3 - c_1 t^2 + c_1^2 t \right) + 1 \right]^2}$$

$$\pi KR_0 = K'$$

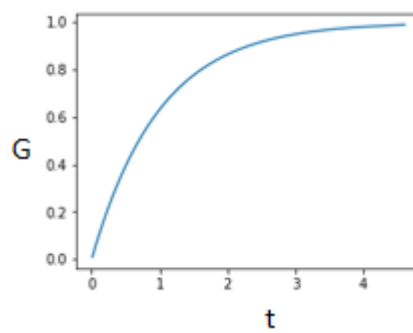
$$G = 1 - \frac{1}{\left[K' \left(\frac{1}{3} t^3 - c_1 t^2 + c_1^2 t \right) + 1 \right]^2}$$



1.6 F -constant (2D)

$$\frac{dG}{dt} = KF(1-G) = K_1(1-G)$$

$$-\ln(1-G) = K_1 t$$

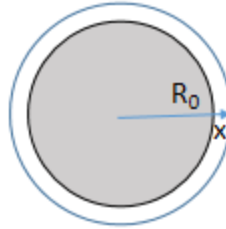


2. Diffusion-controlled

According to the Fick's law,

$$\frac{dm}{dt} = D \left(\frac{dc}{dx} \right)_{x=\xi}$$

2.1 Jander's sphere model



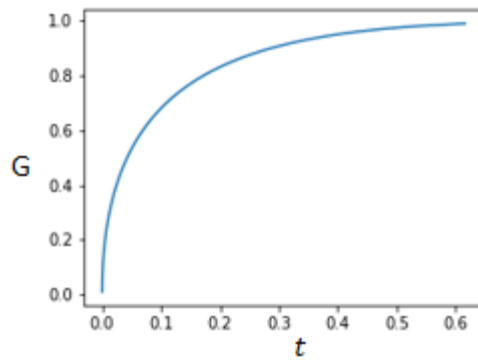
$$G = \frac{V}{V_0} = \frac{\frac{4}{3}\pi R_0^3 - \frac{4}{3}\pi (R_0 - x)^3}{\frac{4}{3}\pi R_0^3} = \frac{R_0^3 - (R_0 - x)^3}{R_0^3}$$

$$x = R_0 [1 - (1 - G)^{\frac{1}{3}}]$$

According to Jander's model, $x^2 = Kt$

$$x^2 = R_0^2 [1 - (1 - G)^{\frac{1}{3}}]^2 = Kt$$

$$[1 - (1 - G)^{\frac{1}{3}}]^2 = \frac{K}{R_0^2} t = K' t$$



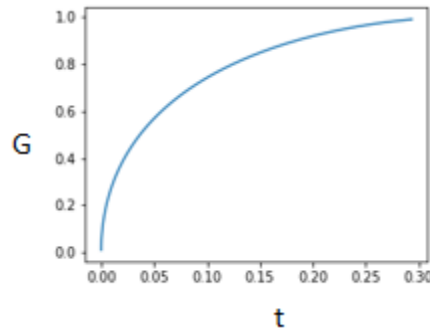
2.2 Ginsterlinger's sphere model

$$G = \frac{V}{V_0} = \frac{\frac{4}{3}\pi R_0^3 - \frac{4}{3}\pi(R_0 - x)^3}{\frac{4}{3}\pi R_0^3} = \frac{R_0^3 - (R_0 - x)^3}{R_0^3}$$

$$x = R_0[1 - (1 - G)^{\frac{1}{3}}]$$

According to Ginsterlinger's model, $\frac{dx}{dt} = K_0 \frac{R_0}{x(R_0 - x)}$

$$1 - \frac{2}{3}G - (1 - G)^{\frac{2}{3}} = K't$$



2.3 Ginsterlinger's cylinder model

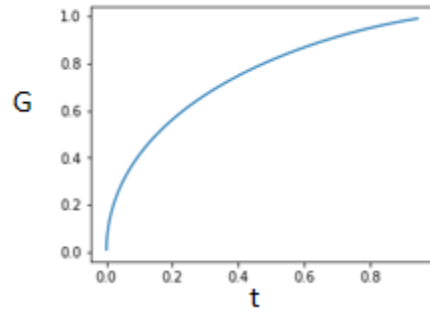
$$dV = [\pi(R_0 - x)^2(h_0 - x)] - [\pi(R_0 - x - dx)^2(h_0 - x - dx)]$$

$$dV = \pi[3x^2 - (4R_0 + 2h_0)x + R_0^2 + 2R_0h_0]dx$$

$$\frac{dm}{dt} = \frac{\rho dV}{dt} = \frac{\pi\rho[3x^2 - (4R_0 + 2h_0)x + R_0^2 + 2R_0h_0]dx}{dt} = D \frac{c_0}{x}$$

$$G = 1 - \frac{V_1}{V_0} = 1 - \frac{\pi(R_0 - x)^2(h_0 - x)}{\pi R_0^2 h_0} = 1 - \left(1 - \frac{x}{R_0}\right)^2 \left(1 - \frac{x}{h_0}\right)$$

$$\ln(1 - G) \cdot (1 - G) + G = K't$$



2.4 Plate model

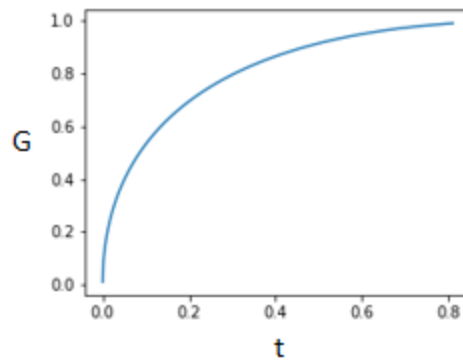
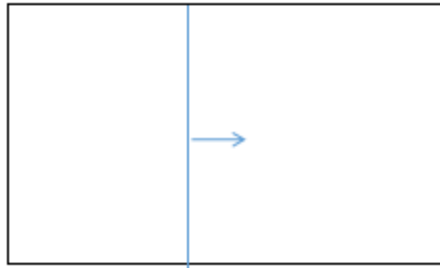
For Jander's diffusion model, the x is proportional to the $t^{\frac{1}{2}}$ in diffusion process

$$x = K_1 t^{\frac{1}{2}}$$

$$G = 1 - \left(1 - \frac{K_1}{R_0} t^{\frac{1}{2}}\right)^2$$

$$\frac{K_1}{R_0} = K'$$

$$G = 1 - (1 - K' t^{\frac{1}{2}})^2$$



2.5 Round plate model

$$dm = 2\pi(R_0 - x)\rho dx$$

According to the Fick's law,

$$\begin{aligned}\frac{dm}{dt} &= D\left(\frac{dc}{dx}\right)_{x=\xi} \\ \frac{dx}{dt} &= \frac{D}{2\pi\rho(R_0 - x)}\left(\frac{dc}{dx}\right)_{x=\xi}\end{aligned}$$

$$\left(\frac{dc}{dx}\right)_{x=\xi} = \frac{c_0}{x}$$

$$\frac{dx}{dt} = \frac{D}{2\pi\rho(R_0 - x)} \frac{c_0}{x} = \frac{Dc_0}{2\pi\rho x(R_0 - x)}$$

$$K_1 = \frac{Dc_0}{2\pi\rho}$$

$$x(R_0 - x)dx = K_1 dt$$

$$t = 0, x = 0$$

$$\frac{R_0}{2}x^2 - \frac{1}{3}x^3 = K_1 t$$

$$G = 1 - \frac{(R_0 - x)^2}{R_0^2}$$

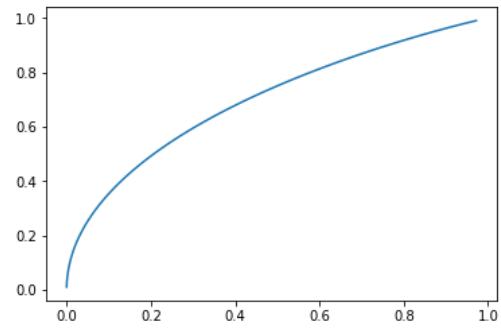
$$x = R_0(1 - \sqrt{1 - G})$$

$$2(1 - G)^{\frac{3}{2}} - 3(1 - G) + 1 = \frac{6K_1}{R_0^3} t$$

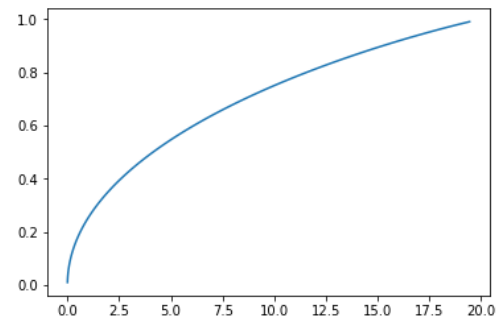
$$K' = \frac{6K_1}{R_0^3} = \frac{3Dc_0}{\pi\rho R_0^3}$$

$$2(1 - G)^{\frac{3}{2}} - 3(1 - G) + 1 = K' t$$

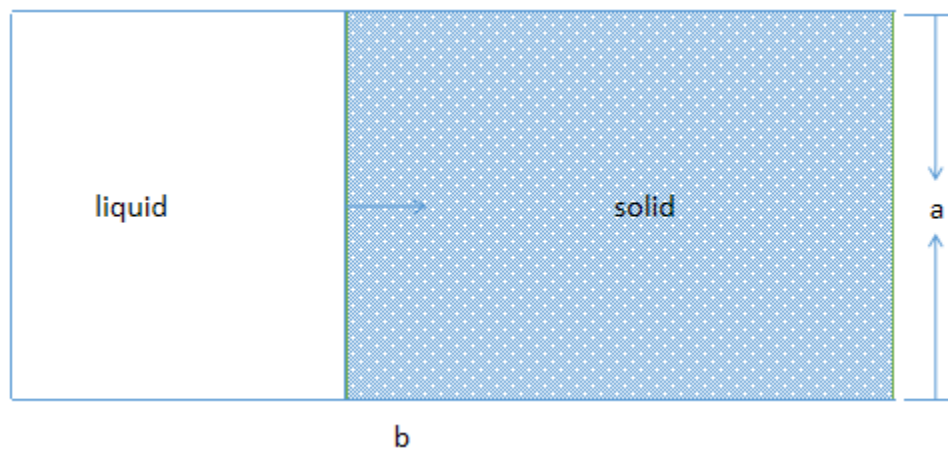
When $K'=1$



When $K' = \frac{1}{20}$



2.6 Constant velocity of reaction interface shift



The liquid-solid interface shift with constant velocity.

$$\frac{dx}{dt} = v$$

(1) For 2D one-way etching process,

$$x = vt$$

$$G = \frac{vt \cdot a}{ab} = \frac{v}{b}t$$

$$\frac{v}{b} = K'$$

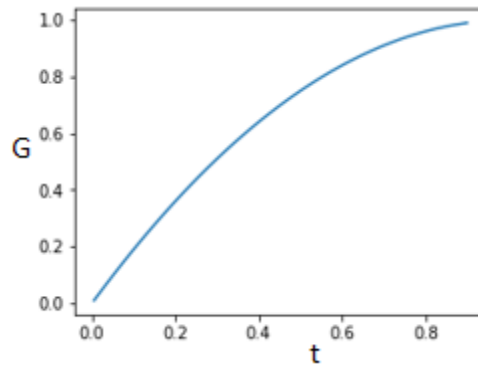
$$G = K't$$

(2) For 2D round plate, $x = vt$, v is the velocity of reaction interface shift.

$$G = 1 - \frac{\pi(R_0 - x)^2}{\pi R_0^2} = 1 - \frac{(R_0 - vt)^2}{R_0^2} = 1 - \left(1 - \frac{v}{R_0}t\right)^2$$

$$\sqrt{1 - G} = 1 - \frac{v}{R_0}t$$

$$1 - \sqrt{1 - G} = \frac{v}{R_0}t = K't$$



For the etching reaction, in the first stage (stage I), the diffusion on the surface is fast (v_D is large), and the surface reaction rate v_R controlled the total reaction. Then in stage II, the diffusion of A atom is the lowest step in the etching process, and controlled the total reaction. In stage III, the number of etching sites increase drastically and the etching shows a self-accelerating characteristic. This is also observed in thermal decomposition. Avrami-Erofeev equation³ is usually employed to describe the self-accelerating reaction.

$$[-\ln(1-G)]^n = kt, n = \frac{1}{2}, \frac{1}{3}$$

Where $n = \frac{1}{2}$ and $n = \frac{1}{3}$ corresponds to two- and three- dimensional reaction respectively. The drawback of the Avrami-Erofeev equation used in etching reaction is that it does not consider the influence of etchant in aqueous environment.

The deduction of parabolic kinetics

For membrane with thickness y , the parabolic relationship of kinetics is deduced as following,

$$\begin{aligned}\frac{dy}{dt} &= \frac{k_p}{y} \\ \int y dy &= \int k_p dt \\ y^2 &= 2k_p t + c\end{aligned}$$

With the increase of membrane thickness, the diffusion of reactant through the membrane is decreased. The reaction rate is inverse ratio with the membrane thickness.

The deduction of Avrami-Erofeev equation³

For a reaction with a constant number of nuclei per unit length (N), or when at the beginning of the reaction a constant number of nuclei is formed immediately (site saturation), and assuming one-dimensional growth, the reaction rate is given by

$$\frac{dG}{dt} = Nk$$

To take overlap of nuclei into account, the right-hand side of equation must be multiplied by (1-G)

$$\frac{dG}{dt} = Nk(1-G)$$

Integration results in

$$-\ln(1-G) = \int Nk dt = \int k_g dt$$

For isothermal reactions k_g is constant, hence

$$-\ln(1-G) = k_g t$$

If nuclei grow isothermally in two dimensions with an equal rate constant for each dimension, and allowing for overlap

$$-\ln(1-G) = C_2 N_2 \left[\int k_1 dt \right]^2 = k_g^2 t^2$$

If nuclei grow isothermally in three dimensions with an equal rate constant for each dimension, and allowing for overlap

$$-\ln(1-G) = C_3 N_3 \left[\int k_1 dt \right]^3 = k_g^3 t^3$$

Reference

1. Slater JC. Atomic Radii in Crystals. *The Journal of Chemical Physics* **41**, 3199-3204 (1964).
2. Miessler GL, Tarr DA. Inorganic chemistry.). Third edition edn. Higher Education Press (2004).
3. De Bruijn TJW, De Jong WA, Van Den Berg PJ. Kinetic parameters in Avrami—Erofeev type reactions from isothermal and non-isothermal experiments. *Thermochim Acta* **45**, 315-325 (1981).